

# THE QUASAR / GALAXY PAIR PKS 1327–206 / ESO 1327–2041: ABSORPTION ASSOCIATED WITH A RECENT GALAXY MERGER

BRIAN A. KEENEY, JOHN T. STOCKE, CHARLES W. DANFORTH

Center for Astrophysics and Space Astronomy, Department of Astrophysical and Planetary Sciences, University of Colorado, 389 UCB,  
Boulder, CO 80309

AND

CHRISTOPHER L. CARILLI

National Radio Astronomy Observatory, P.O. Box O, Socorro, NM 87801

*Draft version June 16, 2019*

## ABSTRACT

We present *HST*/WFPC2 broadband and ground-based H $\alpha$  images, H I 21-cm emission maps, and low-resolution optical spectra of the nearby galaxy ESO 1327–2041, which is located 38'' ( $14 h_{70}^{-1}$  kpc in projection) west of the quasar PKS 1327–206. Our *HST* images clearly show that ESO 1327–2041 is the result of a recent merger that may have ejected a hypercompact galaxy nucleus from the system. Our ground-based H $\alpha$  images reveal the presence of several H II regions in an inclined disk near the galaxy’s center. The WFPC2 images also reveal an extended spiral arm that was previously classified as a polar ring and our optical spectra show H $\alpha$  emission from several H II regions in this arm located  $\sim 5''$  from the quasar position ( $\sim 2 h_{70}^{-1}$  kpc in projection). Absorption associated with ESO 1327–2041 is found in H I 21-cm, optical, and near-UV spectra of PKS 1327–206. We find two absorption components at  $cz_{\text{abs}} = 5255$  and  $5510 \text{ km s}^{-1}$  in the H I 21-cm absorption spectrum, which match the velocities of previously discovered metal-line components. We attribute the  $5510 \text{ km s}^{-1}$  absorber to disk gas in the extended spiral arm and the  $5255 \text{ km s}^{-1}$  absorber to high-velocity gas that has been tidally stripped from the disk of ESO 1327–2041. The complexity of the galaxy/absorber relationships for these very nearby H I 21-cm absorbers suggests that the standard view of high redshift damped Ly $\alpha$  absorbers is oversimplified in many cases.

*Subject headings:* galaxies: interactions — intergalactic medium — quasars: absorption lines

## 1. INTRODUCTION

H I absorption lines in the spectra of background quasars are one of the rare astrophysical phenomena to be discovered first at great distances, where the far-UV Ly $\alpha$  transition redshifts into the optical. Only with the advent of the *Hubble Space Telescope* (*HST*) and its UV spectrographs have we been able to study these absorption lines at low redshift and probe their associations with gas in and around nearby galaxies.

Ly $\alpha$  produces a “forest” of highly-ionized absorption at  $z > 1.8$  in ground-based spectra, as well as the occasional ( $dN/dz \sim 1$ ) high column density ( $17 < \log N_{\text{HI}} < 20.3 \text{ cm}^{-2}$ ) “Lyman-limit systems” (LLSs) and the rare ( $dN/dz \sim 0.1$ ) very high column density ( $\log N_{\text{HI}} \geq 20.3 \text{ cm}^{-2}$ ) “damped Ly $\alpha$  absorbers” (DLAs). Unlike the vast majority of lower column density absorbers, including the LLSs, the DLAs consist of primarily neutral gas and so are potentially more directly related to star formation. Indeed, DLAs represent the largest neutral gas reservoir at each redshift of observation, which has been extended to  $z > 5$  through the discovery of very high- $z$  QSOs and to  $z < 1.8$  using *HST* (Wolfe et al. 2005).

There is no strong evidence for cosmological evolution in  $\Omega_{\text{HI}}$  over that entire range (Prochaska & Herbert-Fort 2004), although there is a factor  $\sim 2$  discrepancy between the lowest redshift DLA  $\Omega_{\text{HI}}$  values and those derived from H I 21-cm emission surveys at  $z \sim$

0 (Zwaan et al. 2005). Further, there are very few DLAs known at  $z < 1.8$  because observing time on *HST* is too restrictive to allow a blind survey for low- $z$  DLAs. A hybrid method of surveying only those QSOs with strong Mg II (and Fe II) absorption has shown some success (Rao, Turnshek, & Nestor 2006; Nestor, Turnshek, & Rao 2005, 2006), but the factor of two discrepancy remains.

High- $z$  DLAs are often modeled as thick gas disks associated with the progenitors of massive spiral galaxies (e.g., Wolfe & Prochaska 2000), but this is largely out of a desire for simplicity since the optical/IR emitting galaxy associated with the DLA is rarely detected, or even detectable, using current ground-based or space-based telescopes. The galaxy population responsible for DLAs is spread over a large range of luminosities ( $0.001\text{--}1 L^*$ ; Zwaan et al. 2005; Rosenberg & Schneider 2003), so it is not surprising that it has been difficult to detect high- $z$  DLA galaxies nor that the spread in DLA metallicities is  $\sim 2$  dex at any given redshift. The  $\log N_{\text{HI}} \geq 20.3 \text{ cm}^{-2}$  limit makes good sense physically since above this limit the gas must be primarily neutral; however, systems with H I column densities just below this limit (sometimes called “sub-DLAs” or “super Lyman limit systems”) may share many of the same associated galaxy properties with the DLAs.

The absence of direct galaxy detection for many DLAs and sub-DLAs is in marked contrast to the situation for LLSs, which are found to be associated with nearby (impact parameter  $\leq 50$  kpc), luminous ( $L \geq 0.1 L^*$ ), gas-

rich galaxies. The high luminosity and proximity of LLS host galaxies to the quasar sight line have been critical to their successful identification (e.g., Steidel 1995; Churchill et al. 2007; Kacprzak et al. 2010). The current consensus model for LLSs is gas in the halo of luminous galaxies although what is meant by “halo” is not clearly defined and can encompass outflowing, unbound winds (Adelberger et al. 2003; Heckman et al. 2001; Martin 1999), outflowing or infalling galactic “fountain” material (Mo & Miralda-Escude 1996; Richter et al. 2009; Keeney et al. 2005; Stocke, Keeney, & Danforth 2010), infalling cold mode accretion clouds (Kereš & Hernquist 2009), or disrupted satellites (York et al. 1986).

Discovery surveys for new low- $z$  absorber/galaxy associations, particularly DLAs and sub-DLAs, are needed to better resolve the associated galaxy from the QSO, to clearly detect the lower luminosity examples of associated galaxies, and to study the associated galaxy properties using all available ground-based and space-based techniques. To this end we initiated a modest-sized *HST* imaging project to study the detailed absorber/galaxy relationship for three very low- $z$  ( $cz \leq 10,000 \text{ km s}^{-1}$ ) H I 21-cm absorbers: 3C 232/NGC 3067, PKS 1327–206/ESO 132722–2040.6 (hereafter ESO 1327–2041), and PKS 2020–370/Klemola 31A. While each of these systems was initially discovered using H I 21-cm absorption (which is only sensitive to DLAs and sub-DLAs) against a background radio-loud quasar, two of the three (the first two above) were also detected in Ca II H & K and Na I D absorption by ground-based telescopes (Boksenberg & Sargent 1978; Stocke et al. 1991; Kunth & Bergeron 1984; Bergeron, Kunth, & D’Odorico 1987). Carilli & van Gorkom (1992, CvG92 hereafter) have used the Very Large Array (VLA) to map each of these systems in H I 21-cm emission for comparison to the absorption line data.

In a previous paper (Stocke et al. 2010), we presented our new *HST* imaging of the 3C 232/NGC 3067 system which allowed us to conclude that the H I 21-cm sub-DLA absorber in the spectrum of that quasar is very similar in its physical properties to high-velocity clouds (HVCs) found around the Milky Way (Keeney et al. 2005). We also found that this gas is infalling onto the disk of NGC 3067. The simplicity of this QSO/galaxy pair — relatively isolated galaxy viewed at an intermediate inclination angle — allowed for an easy interpretation of the cloud kinematics and properties.

In this paper we present our *HST* imaging results for the second pair, PKS 1327–206/ESO 1327–2041, a much more complex galaxy system with polar ring H I gas, which we show is likely due to a direct galaxy collision between a gas poor lenticular galaxy and a late-type spiral. The quasar absorber consists of two velocity components separated by  $\sim 250 \text{ km s}^{-1}$  in both metal lines and H I 21-cm absorption. However, Ly $\alpha$  itself in this system is not directly observable due to a high- $z$  LLS, so we do not know for certain whether this absorber complex is a DLA or a sub-DLA. Regardless, this absorber/galaxy pair clearly shows the potential complexity of such systems.

We have obtained new VLA H I 21-cm emission maps, a new H I 21-cm absorption spectrum, ground-based H $\alpha$  imaging and long-slit spectroscopy of various galaxy components, as well as a new optical spectrum of the quasar

at moderate ( $\sim 2 \text{ \AA}$ ) resolution, in addition to the aforementioned *HST* continuum imaging of this  $\sim L^*$  galaxy merger at  $z = 0.0178$  ( $cz \approx 5500 \text{ km s}^{-1}$ ). We also present an archival *HST*/FOS spectrum of PKS 1327–206 which detects several near-UV metal lines including Mg I, Mg II, Fe II, and Mn II at the redshift of ESO 1327–2041. In §2 we present the new *HST* and ground-based images, the H I 21-cm emission maps, and the optical spectra of various regions in ESO 1327–2041. In §3 we show the H I 21-cm, optical, and near-UV spectra of the quasar PKS 1327–206 that we have analyzed. In §4 we speculate on the nature of a nearly unresolved knot of starlight emission discovered in our *HST* images which may be a hyper-compact galaxy nucleus ejected from ESO 1327–2041 as a result of the galaxy collision now on-going. In §5 we summarize the results of our observational campaign on this system and discuss the importance of this system for interpreting high- $z$  DLAs and sub-DLAs. We assume  $h_{70} = H_0/(70 \text{ km s}^{-1} \text{ Mpc}^{-1})$  and a distance to ESO 1327–2041 of  $80 \pm 5 h_{70}^{-1} \text{ Mpc}$  throughout this paper.

## 2. THE INTERACTING GALAXY PAIR ESO 1327–2041

Early CCD images of ESO 1327–2041 revealed its disturbed optical morphology, which includes an elongated nucleus (oriented roughly north-south) with a central bulge, an east-west “polar ring” that extends from the galaxy nucleus to the quasar position, and a bright plume that extends  $45''$  northeast of the galaxy nucleus (Giraud 1986). Subsequent H I 21-cm emission maps of ESO 1327–2041 confirmed the presence of a regularly-rotating gaseous ring extending in the direction of PKS 1327–206 (CvG92). This complex morphology suggests that ESO 1327–2041 is the result of a recent major merger and/or a significant tidal interaction and that any absorption lines probing this system will also be quite complex.

We have obtained high-resolution observations of ESO 1327–2041 at multiple wavelengths, allowing us to study this galaxy in unprecedented detail. These observations include: *HST* broadband (§2.1) and ground-based H $\alpha$  images (§2.2) of ESO 1327–2041, H I 21-cm emission maps of ESO 1327–2041 and PKS 1327–206 (§2.3), and long-slit optical spectra of several regions of ESO 1327–2041 (§2.4).

### 2.1. Broadband *HST* Images

ESO 1327–2041 was observed with the Wide-Field Planetary Camera 2 (WFPC2) on board *HST* on 16 Apr 2007 for a total of 4200 s in the F675W (*R*-band) filter and 2400 s in each of the F450W (Wide *B*-band) and F791W (Wide *I*-band) filters as part of GO program 10925 (PI: J. Stocke). The images were reduced and coadded using the *stsdas* package of IRAF, as described in the WFPC2 Data Handbook<sup>1</sup>. The orientation of our observations were such that ESO 1327–2041 and PKS 1327–206 fell only on WF2 and WF3, so we did not analyze the WF4 or PC chips of the detector. Our reduced images reach limiting  $3\sigma$  Vega magnitudes of 26.9, 26.5, and 26.0 for point sources in the F450W, F675W, and F791W filters, respectively.

<sup>1</sup> The WFPC2 Data Handbook can be found at <http://www.stsci.edu/hst/wfpc2/>.

A color composite image of the WFPC2 data (WF2 and WF3 chips only) is shown in the left panel of Figure 1, where the F450W data are displayed in blue, the F675W data in green, and the F791W data in red. The lower-resolution red areas in the center of ESO 1327–2041 are H II regions detected in our ground-based H $\alpha$  images (§ 2.2). The field-of-view of Figure 1 is approximately  $75'' \times 150''$ , which corresponds to a physical scale of  $\sim 28 \times 56 h_{70}^{-1}$  kpc at the redshift of ESO 1327–2041.

All of the features identified by Giraud (1986) and CvG92 are present in the WFPC2 images, but the superior spatial resolution of *HST* reveals several new features that we have labelled in a schematic of the WFPC2 images in the right panel of Figure 1. In particular, the central region of ESO 1327–2041 is resolved into two components that are blended together at ground-based resolution: a lenticular component that corresponds to the “elongated nucleus” of Giraud (1986), and an inclined spiral that contains several H II regions. These components are clearly co-spatial since H II regions in the spiral disk are seen in front of the starlight from the lenticular component to the south of the galaxy nucleus but are occulted by the lenticular starlight to the north of the nucleus (i.e., the inclined disk is seen both in front of and behind the lenticular component). The “plume” of material extending NNE from the galaxy nucleus is resolved into a stellar stream with a compact embedded source that we speculate in § 4 is the ejected nucleus of the inclined spiral. There is also a small companion galaxy located just north of the stellar stream, approximately halfway between the embedded source and the lenticular nucleus.

The previously identified “polar ring” is now resolved to be the outermost arm of the inclined spiral in the central regions of ESO 1327–2041. This arm may be in the process of being tidally stripped and passes quite close to the PKS 1327–206 sight line. We have detected several H II regions in this extended arm located  $\sim 5''$  ( $\sim 2 h_{70}^{-1}$  kpc) north of PKS 1327–206 (see Fig. 1 and § 2.4).

CvG92 found that the gas in the “polar ring” of ESO 1327–2041 is rotating regularly with lower velocities ( $\sim 5250$  km s $^{-1}$ ) in the west and higher velocities ( $\sim 5500$  km s $^{-1}$ ) in the east. This rotation is not surprising since we now identify this feature with an extended spiral arm. However, whether we call the gas that extends from the galaxy nucleus in the direction of PKS 1327–206 a “polar ring” or an “extended spiral arm” is largely a matter of semantics since the standard picture of polar-ring galaxies is that they are formed via galaxy mergers or the accretion of a companion galaxy or IGM filament (Moiseev & Bizyaev 2009; Bournaud & Combes 2003).

## 2.2. H $\alpha$ Images

Ideally, we would have obtained H $\alpha$  images of ESO 1327–2041 with *HST* as well, but neither WFPC2 nor ACS had a narrowband filter suitable for observing H $\alpha$  at the redshift of ESO 1327–2041. Instead the galaxy was observed at Apache Point Observatory (APO) on 24 Mar 2006 using the SPICAM imager of the ARC 3.5-m telescope. Redshifted H $\alpha$  + [N II] images were obtained in  $1''.3$  seeing for a total of 3000 s using a filter with a

central wavelength of 6650 Å and FWHM = 80 Å. Additionally, ESO 1327–2041 was observed for 1800 s in  $1''.4$  seeing through an off-band filter with FWHM = 100 Å and a central wavelength of 6450 Å in order to measure the strength of the stellar continuum. All images were reduced and coadded using standard IRAF procedures. The off-band image was then scaled so that its sky level matched that of the H $\alpha$  on-band image before continuum subtraction. The resulting image should only contain flux from the H $\alpha$  and [N II] emission lines, but there is some residual flux in the cores of bright stars due to the slight mismatch in seeing between the on-band and off-band images. Our final continuum-subtracted H $\alpha$  image has been overlaid in red on the WFPC2 data in Figure 1. Only pixels with  $F(\text{H}\alpha) > 10^{-17}$  ergs s $^{-1}$  cm $^{-2}$  are shown, corresponding to areal star formation rates  $> 0.005 h_{70}^{-2} M_{\odot} \text{yr}^{-1} \text{kpc}^{-2}$  at the distance of ESO 1327–2041 (Kennicutt 1998).

Figure 1 clearly highlights several H II regions in the inclined spiral disk of ESO 1327–2041. These H II regions have an integrated H $\alpha$  flux of  $F(\text{H}\alpha) = (7.2 \pm 1.4) \times 10^{-14}$  ergs s $^{-1}$  cm $^{-2}$  assuming a [N II]/H $\alpha$  ratio of  $0.3 \pm 0.2$  (derived as in Kennicutt et al. 2008). At our assumed distance to ESO 1327–2041 of  $80 \pm 5 h_{70}^{-1}$  Mpc, this corresponds to a luminosity of  $(5.5 \pm 1.3) \times 10^{40} h_{70}^{-2}$  ergs s $^{-1}$  and a star formation rate of  $0.44 \pm 0.10 h_{70}^{-2} M_{\odot} \text{yr}^{-1}$  (Kennicutt 1998). So, despite the morphological evidence for a significant merger event in the recent past of ESO 1327–2041, this interaction is not currently driving a major starburst episode.

The semi-stellar knots just NNW of PKS 1327–206 (labelled as H II regions in the right panel of Fig. 1) show no obvious H $\alpha$  emission in our narrowband images. Nevertheless, a deep long-slit optical spectrum clearly detects very weak H $\alpha$  emission associated with these knots (see § 2.4), solidifying our earlier identification.

## 2.3. H I 21-cm Emission Maps

ESO 1327–2041 and PKS 1327–206 were observed by the Very Large Array (VLA) in the CnB configuration for 18.74 hours between 18 Jun and 4 Jul 2005. Data were obtained in L-band (1.4 GHz) centered at a heliocentric velocity<sup>2</sup> of 5370 km s $^{-1}$  using 63 spectral channels with a width of 10.4 km s $^{-1}$  (48.8 kHz) per channel. To improve sensitivity and resolution, these data were combined with the data of CvG92 after flagging and calibration. The CvG92 data were obtained with the VLA C-array on 20 Dec 1990 with the same channel configuration described above. The addition of the CvG92 data increases the total exposure time of our observations to 25.8 hours. All reductions for both data sets were performed with the Common Astronomy Software Applications (CASA) Beta Release, Version 2.0.

Figure 2 shows H I 21-cm (blue) and 1.4-GHz continuum (green) emission contours overlaid on the F675W WFPC2 data. The large red ellipse in the upper-left corner of the image is the restoring beam of the natural-weighted H I contours and the smaller ellipse is the restoring beam of the uniform-weighted continuum con-

<sup>2</sup> We have reduced the VLA data using the optical definition of velocity,  $v/c = (\nu_0 - \nu)/\nu = (\lambda - \lambda_0)/\lambda_0 = z$ , rather than the traditional radio definition.

tours. PKS 1327–206 has a double-lobed morphology and a peak continuum flux of  $280 \text{ mJy beam}^{-1}$  at this resolution. There is also a weak continuum source (peak flux  $\sim 5 \text{ mJy beam}^{-1}$ ), first detected by CvG92, located  $\sim 10''$  south of the embedded object in the stellar stream (see Fig. 1) that Figure 2 reveals is associated with a background galaxy and not the embedded object itself.

Continuum sources were subtracted from the data cube before imaging the H I emission using the CASA task `uvcontsub` to perform a channel-by-channel linear fit to the continuum. We believe that the hole in the H I distribution toward PKS 1327–206 is due to the H I 21-cm absorption against the quasar background (see §3.1). The H I contours in Figure 2 show three peaks: one (labelled “A” in Fig. 2) near the nucleus of the lenticular component of ESO 1327–2041 and two (“B” and “C”) that are likely associated with the extended spiral arm. There is also a region of more diffuse emission (“D”) that extends in the direction of the stellar stream but is offset approximately one beam width to the east and, finally, a large diffuse region (“E”) near the northern edge of the image.

Table 1 lists the positions, velocities, and H I masses of these regions. We find that gas in the extended spiral arm is rotating regularly with lower velocities in the south and west (regions A & C) and higher velocities in the north and east (region B). The more diffuse extended regions of H I 21-cm emission (regions D & E) have velocities that are  $\sim 150 \text{ km s}^{-1}$  lower than the closest disk gas in region B.

Figure 2 can be used to determine how the recent merger history of ESO 1327–2041 has affected its 21-cm emission properties compared to more isolated galaxies. The H I-emitting regions of typical spiral galaxies extend about twice as far as the regions of optical emission (e.g., Broeils & Rhee 1997; Noordermeer et al. 2005), which suggests that the “pre-merger” H I extent of ESO 1327–2041 was  $\sim 60''$  ( $\sim 23 h_{70}^{-1} \text{ kpc}$ ). The measured angular extent of regions A–C in Figure 2 is  $\sim 60''$ , but increases to  $\sim 80''$  ( $\sim 31 h_{70}^{-1} \text{ kpc}$ ) if region D is included. Thus, the size of the H I-emitting region of ESO 1327–2041 has increased only modestly as a result of its recent interaction.

However, the galaxy interaction *has* caused ESO 1327–2041 to become noticeably H I-deficient as compared to more isolated galaxies. The total H I mass of regions A–E of ESO 1327–2041 is  $M_{\text{HI}} = (9.6 \pm 0.6) \times 10^8 M_{\odot}$  (see Table 1), but late-type spirals with the same luminosity and optical size as ESO 1327–2041 tend to have H I masses of  $M_{\text{HI}} \sim 4 \times 10^9 M_{\odot}$  (Haynes & Giovanelli 1984). This deficiency can easily be explained if most of the H I in ESO 1327–2041 was ionized during the interaction. Ionization considerations may also explain why the interaction failed to dramatically increase the H I extent of ESO 1327–2041.

#### 2.4. Optical Spectra

ESO 1327–2041 was observed with the DIS spectrograph of the ARC 3.5-m telescope at APO on 1 May 2008 and 27–28 Feb 2009 using a  $1''.5$  slit and the B400+R300 gratings. These gratings cover the wavelength range  $3600\text{--}9000 \text{ \AA}$  at  $6\text{--}7 \text{ \AA}$  resolution except for a gap from  $\sim 5300\text{--}5700 \text{ \AA}$  caused by a dichroic in the spectrograph. Data were obtained at three different slit positions: the

first slit position was oriented along the major axis of the lenticular component of ESO 1327–2041, the second position was along the stellar stream with the slit passing through the embedded compact object, and the third position connected the compact object embedded in the stellar stream and PKS 1327–206 with the slit also passing through the H II regions in the extended spiral arm. Observations of Feige 34 taken each night were used for flux calibration, and all data were reduced with a combination of standard IRAF tasks and custom IDL routines.

The DIS spectrograph has a spatial scale of  $0''.4$  per pixel, and extraction apertures of  $10''$ ,  $40''$ , and  $5''$  were used for the lenticular component of ESO 1327–2041, the stellar stream, and the source embedded in the stream, respectively. The spectra of these galaxy components are shown in Figure 3. Only the blue portion of the spectra are shown, and the flux levels have been arbitrarily scaled for ease of display. The vertical dashed lines indicate the positions of the  $\text{H}\beta\text{--H}\eta$  absorption lines detected in the spectrum of the embedded source. There are indications of even higher-order Balmer absorption from  $\text{H}\theta$ ,  $\text{H}\iota$ , and  $\text{H}\kappa$  in the spectrum of the embedded source, but declining signal-to-noise blueward of  $3800 \text{ \AA}$  precludes us from making positive identifications.

Tables 2–4 list the line identification, rest wavelength, observed wavelength, heliocentric velocity, and rest-frame equivalent width of all lines detected in the DIS spectra, including lines detected at wavelengths not displayed in Figure 3. For the emission lines detected in the lenticular nucleus, Table 4 lists integrated line fluxes instead of rest-frame equivalent widths. These fluxes have not been corrected for Galactic or intrinsic reddening. Rest wavelengths for these and all other Tables were taken from the Atomic Line List<sup>3</sup>.

Examination of these Tables shows that Ca II H & K absorption lines are detected in all three spectra, that the embedded source is detected primarily in Balmer absorption lines, and that the lenticular component is detected mostly in nebular emission with some absorption from an older stellar population. Further, the absorption lines detected in the three spectra indicate a clear hierarchy in the age of their stellar populations with the embedded source being the youngest, the stellar stream intermediate in age, and the lenticular nucleus the oldest.

There is also a significant velocity difference between the emission and absorption lines detected in the lenticular component of ESO 1327–2041, suggesting that the emission lines are associated with a foreground H II region (see Table 4). The nebular emission-line velocity of this H II region ( $5380 \pm 10 \text{ km s}^{-1}$ ) is similar to the peak H I 21-cm emission velocity of region A ( $5338 \text{ km s}^{-1}$ ; see Table 1 and Fig. 2), the nearest H I 21-cm peak to the lenticular nucleus, confirming our earlier identification of the H I 21-cm emission peaks A–C with spiral disk gas. The absorption-line velocity in Table 4 ( $5460 \pm 20 \text{ km s}^{-1}$ ) then represents the velocity of the lenticular nucleus itself.

We have detected very weak  $\text{H}\alpha$  emission from the H II regions in the extended spiral arm at our third slit position. These H II regions, which are heavily blended at

<sup>3</sup> The Atomic Line List is hosted by the Department of Physics and Astronomy at the University of Kentucky (see <http://www.pa.uky.edu/~peter/newpage/>).

ground-based resolution, are located  $\sim 5''$  ( $\sim 2 h_{70}^{-1}$  kpc) north of PKS 1327–206 (see Fig. 1) and have a heliocentric velocity of  $5440 \pm 20 \text{ km s}^{-1}$ . Examination of their 2D spectrum reveals a velocity gradient across the H $\alpha$  blend that we have extrapolated to the position of PKS 1327–206 to estimate the disk velocity at the quasar position to be  $5500 \pm 30 \text{ km s}^{-1}$ . This estimate is close to the H I 21-cm emission velocity near the quasar position, which ranges from  $\sim 5400\text{--}5490 \text{ km s}^{-1}$  (CvG92).

### 3. ABSORPTION LINES ASSOCIATED WITH ESO 1327–2041 IN THE SPECTRUM OF PKS 1327–206

Past studies of the optical and radio spectra of PKS 1327–206 have found absorption associated with the nearby galaxy ESO 1327–2041 ( $cz_{\text{gal}} = 5380 \pm 10 \text{ km s}^{-1}$ ). A high-resolution ( $v_{\text{res}} \approx 30 \text{ km s}^{-1}$ ) optical spectrum obtained by Bergeron et al. (1987) revealed two velocity components in the Na I D doublet at  $5250 \pm 10$  and  $5490 \pm 10 \text{ km s}^{-1}$ . A lower resolution ( $v_{\text{res}} \approx 225 \text{ km s}^{-1}$ ) optical spectrum, also from Bergeron et al. (1987), showed Ca II H & K absorption at  $5340 \pm 90 \text{ km s}^{-1}$ . CvG92 also found two velocity components in the H I 21-cm absorption spectrum of PKS 1327–206, although their detection of the  $5490 \text{ km s}^{-1}$  component was tentative due to potential confusion from emission in the beam.

We have acquired more sensitive H I 21-cm and optical spectra of PKS 1327–206, which we present in §3.1 and §3.2, respectively. We have also analyzed an archival *HST* near-UV (NUV) spectrum of PKS 1327–206, which is presented in §3.3 and Appendix A. These spectra allow us to confirm the presence of two H I 21-cm absorbers, search for evidence of absorption from both velocity components in the Ca II H & K line profiles, and determine whether any gas associated with ESO 1327–2041 is present in the NUV spectrum of PKS 1327–206.

#### 3.1. H I 21-cm Spectrum

Our VLA observations (§2.3) allow us to search for H I 21-cm absorption against the quasar continuum in addition to studying the H I 21-cm emission properties of ESO 1327–2041. The H I 21-cm absorption spectrum of PKS 1327–206 is shown in Figure 4 with Gaussian fits to the absorption lines overlaid with thick black lines. The dashed vertical lines show the velocities of the Na I D absorption components found by Bergeron et al. (1987), which clearly match the 21-cm absorption velocities. Table 5 lists best-fit physical parameters derived from the Gaussian fits to the H I absorption components in Figure 4.

The H II regions just NNW of PKS 1327–206 (see Fig. 1) have heliocentric velocities comparable to the  $5510 \text{ km s}^{-1}$  H I absorption complex. An extrapolation of the H $\alpha$  emission line velocities towards PKS 1327–206 (see §2.4) arrives at the velocity indicated by the dotted vertical line in Figure 4. From this extrapolation we identify the  $5510 \text{ km s}^{-1}$  H I 21-cm absorber with the extended spiral arm of ESO 1327–2041, and thus as galactic disk absorption. The velocity of the H I 21-cm emission near the position of PKS 1327–206 is also compatible with this interpretation (CvG92).

CvG92 identified very weak H I 21-cm emission aligned with the stellar stream of ESO 1327–2041 and extending

much further to the north (see their Figs. 3 and 4), but at significantly lower spatial resolution ( $50''$ ) than we show in Figure 2. Regions D & E in Figure 2 are the densest regions of this very diffuse emission, which extends into the vicinity of PKS 1327–206 at velocities between  $5190$  and  $5296 \text{ km s}^{-1}$  (CvG92). CvG92 suggest that the H I 21-cm absorber at  $5255 \text{ km s}^{-1}$  arises in this low surface brightness gas. Given the complex optical and H I 21-cm morphology of ESO 1327–2041, we hypothesize that the  $5255 \text{ km s}^{-1}$  absorber represents gas that has been tidally stripped from the disk of ESO 1327–2041.

The  $5255 \text{ km s}^{-1}$  absorber in Figure 4 is spectroscopically unresolved, so we attempted to use it to correct the width of the  $5510 \text{ km s}^{-1}$  absorber for the effects of instrumental resolution, allowing us to estimate its kinetic temperature. However, the resulting kinetic temperature estimate was  $\sim 55,000 \text{ K}$ , which is unphysically large (H II regions have typical temperatures of  $\sim 10,000 \text{ K}$ ; e.g., Anderson et al. 2009), implying that the width of the  $5510 \text{ km s}^{-1}$  absorber is caused by velocity structure rather than thermal broadening. The non-Gaussian shape of the  $5510 \text{ km s}^{-1}$  absorber also suggests the presence of multiple velocity components as is seen in our own Galactic plane. If the width of this absorber can be attributed to velocity structure along the line of sight, then the extended spiral arm has a velocity dispersion of  $\sim 25 \text{ km s}^{-1}$  at the quasar position.

The strength of H I 21-cm absorption depends on the column density ( $N_{\text{HI}}$ ), covering fraction ( $f$ ), and spin temperature ( $T_{\text{spin}}$ ) of the absorbing gas (see Table 5). Assuming  $T_{\text{spin}} \sim 100 \text{ K}$  (typical of the cold neutral medium in spiral galaxy disks; e.g., Roy, Chengalur, & Srianand 2006) and  $f = 1$ , the column density of the  $5255 \text{ km s}^{-1}$  absorber is  $N_{\text{HI}} \sim 2 \times 10^{19} \text{ cm}^{-2}$  and the column density of the  $5510 \text{ km s}^{-1}$  absorber is  $N_{\text{HI}} \sim 4 \times 10^{19} \text{ cm}^{-2}$ . These column densities are clearly uncertain due to ambiguities in both the spin temperature and covering factor of the absorbing gas. However, since a higher spin temperature indicative of halo gas (see, e.g., Keeney et al. 2005) and/or a smaller covering factor would tend to **increase** the derived column density, these estimates nevertheless suggest that the two 21-cm absorbers can plausibly combine to form a DLA as one would expect to find in a quasar sight line that passes within  $15 h_{70}^{-1}$  kpc of a foreground galaxy.

#### 3.2. Optical Quasar Spectrum

Bergeron et al. (1987) argued that the observed Ca II/Na I ratio ( $\mathcal{W}_{\lambda}(\text{Ca II})/\mathcal{W}_{\lambda}(\text{Na I}) = 0.34$  for the  $5255$  and  $5510 \text{ km s}^{-1}$  absorbers combined) points toward a galactic disk origin for the absorbing gas. However, since their Ca II spectrum does not resolve both of the velocity components that they detected in Na I, they cannot assess the origin of the individual absorbers directly. Therefore, we obtained high-resolution optical spectra of PKS 1327–206 near the Ca II H & K ( $v_{\text{res}} \approx 150 \text{ km s}^{-1}$ ) and Na I D ( $v_{\text{res}} \approx 75 \text{ km s}^{-1}$ ) absorption lines associated with ESO 1327–2041 to study the Ca II / Na I ratio of the individual velocity components.

ESO 1327–2041 was observed with the DIS spectrograph of the ARC 3.5-m telescope at APO on 10 Feb 2010, 4 Apr 2010, and 6 May 2010 using a  $1''.5$  slit

and the B1200+R1200 gratings. At central wavelengths of 4500 and 6400 Å, these gratings cover the wavelength ranges from 3900–5100 Å and 5800–7000 Å at 2 Å resolution. Observations of Feige 34 taken each night were used for flux calibration, and all data were reduced with a combination of standard IRAF tasks and custom IDL routines.

The regions surrounding the Ca II H & K and Na I D absorption lines associated with ESO 1327–2041 are shown in Figure 5. Two velocity components are clearly detected in the Na I D doublet, with the Na I D1 line of the bluer component blended with the Na I D2 line of the redder component. Best-fit velocities, column densities, and deconvolved equivalent widths of these components were determined by simultaneous Voigt profile fits to the Na I D doublets, assuming a fixed Doppler parameter of  $b = 15 \text{ km s}^{-1}$ . The velocity structure of the Ca II profiles is less clear, but an apparent optical depth analysis of the Ca II K profile shows two significant peaks, which we use to measure the velocities and calculate the apparent column densities of both components (Sembach & Savage 1992). Deconvolved equivalent widths were then calculated from the apparent column densities assuming optically thin absorption, and simulated Ca II absorption line profiles were calculated assuming  $b = 15 \text{ km s}^{-1}$ .

The simulated Ca II and best-fit Na I absorption line profiles have been overlaid on the data in Figure 5. Table 6 lists the line identification, rest wavelength, observed wavelength, heliocentric velocity, and rest-frame equivalent widths derived from these profiles. The Ca II and Na I velocities clearly agree with each other, as well as with the velocities of the H I 21-cm components.

The 5255 and 5510  $\text{km s}^{-1}$  velocity components have  $\mathcal{W}_\lambda(\text{Ca II})/\mathcal{W}_\lambda(\text{Na I})$  ratios of  $0.26 \pm 0.16$  and  $0.63 \pm 0.15$ , respectively, and a combined ratio of  $0.48 \pm 0.11$  (slightly higher than the value found by Bergeron et al. 1987). Ratios this low require a weak ionizing radiation field and are typically associated with disk gas in our Galaxy (Morton & Blades 1986), whereas larger values ( $\mathcal{W}_\lambda(\text{Ca II})/\mathcal{W}_\lambda(\text{Na I}) \gtrsim 1$ ) indicate a stronger radiation field associated with a galactic halo environment (e.g., Morton & Blades 1986; Stocke et al. 1991). A disk gas origin for both velocity components suggests that the 5255  $\text{km s}^{-1}$  component represents gas that has been tidally stripped from the disk of ESO 1327–2041 rather than a high-velocity infalling or outflowing cloud in the halo of the galaxy.

### 3.3. *HST* Near-UV Spectrum

PKS 1327–206 was observed with the Faint Object Spectrograph (FOS) on board *HST* on 13 Jan 1997 for a total of 6540 s with the G270H grating as part of GO program 5654. These data were taken through the 1'0 aperture<sup>4</sup> and cover a wavelength range of 2222–3277 Å at 2 Å ( $\sim 200 \text{ km s}^{-1}$ ) resolution. The FOS spectrum of PKS 1327–206 is filled with absorption lines from many redshifts, including Galactic ISM lines, lines associated with ESO 1327–2041, lines associated with the Lyman-limit system (LLS) at  $z = 0.85238$  (Bergeron et al. 1987),

<sup>4</sup> The actual size of the aperture is 0'86 since these observations were obtained after the installation of COSTAR on *HST*.

and intergalactic Ly $\alpha$  forest absorbers. We discuss the lines associated with ESO 1327–2041 here and defer discussion of the other absorption lines in the PKS 1327–206 spectrum to Appendix A since this spectrum has not been discussed previously in the literature.

Table 7 lists the line identification, rest wavelength, observed wavelength, heliocentric velocity, and rest-frame equivalent width of all absorption lines associated with ESO 1327–2041 that were detected at  $> 4\sigma$  confidence (observed  $\mathcal{W}_\lambda > 200 \text{ mÅ}$ ) in the *HST*/FOS spectrum of PKS 1327–206<sup>5</sup>. The average velocity centroid of this absorption line system is  $5360 \pm 10 \text{ km s}^{-1}$ , which is intermediate in velocity to the two H I 21-cm components. In addition to the lines listed in Table 7, the FOS spectrum shows indications of Mn II  $\lambda 2577$  and Mn II  $\lambda 2606$  absorption associated with ESO 1327–2041 at  $2-3\sigma$  confidence.

Figure 6 shows the absorption line profiles of all of the lines listed in Table 7. Lines marked with a “G” are Galactic ISM lines and those marked with solid vertical lines are associated with the LLS at  $z = 0.85238$ . The dashed vertical lines show the velocities of the H I 21-cm absorbers at 5255 and 5510  $\text{km s}^{-1}$ . Unfortunately, the velocity resolution of the FOS spectrum is comparable to the separation of the 21-cm velocity components. Given that the average velocity centroid of the NUV line profiles is intermediate to the H I 21-cm absorber velocities, it is likely that they represent blended absorption from both of the 21-cm velocity components.

### 3.4. *Summary of Absorption Lines Associated with ESO 1327–2041*

Two velocity components at 5255 and 5510  $\text{km s}^{-1}$  have been detected in H I 21-cm, Ca II, and Na I absorption, and the low-resolution NUV absorption line profiles of Fe II, Mn II, Mg I, and Mg II likely represent blended absorption from both components. The 5510  $\text{km s}^{-1}$  absorber is coincident in velocity with disk gas in the extended spiral arm of ESO 1327–2041 at the location of PKS 1327–206 as traced by H I 21-cm emission (CvG92) and H II regions in the arm (§ 2.4). The low Ca II/Na I ratio of this component also suggests a galactic disk origin for the absorbing gas.

The origins of the 5255  $\text{km s}^{-1}$  component are less clear. It has an unresolved H I 21-cm absorption line profile and its Ca II/Na I ratio is even lower than that found for the 5510  $\text{km s}^{-1}$  component, both of which suggest that the 5255  $\text{km s}^{-1}$  absorber is cold disk gas with a simple line-of-sight velocity structure. However, the velocity of this component differs from the disk velocity at the quasar position by  $\sim 250 \text{ km s}^{-1}$ , which would usually imply a high-velocity cloud origin for the absorbing gas. We believe that the 5255  $\text{km s}^{-1}$  component represents gas that was tidally stripped from the western side of the inclined spiral disk of ESO 1327–2041 as a result of a past merger and now resides in the very diffuse tidal tail detected in H I 21-cm emission near the position of PKS 1327–206 (CvG92). This origin simultaneously explains the disk gas signatures and high-velocity cloud

<sup>5</sup> To ensure that Galactic ISM lines were centered at  $v_{\text{helio}} \sim 0$  we applied a zero-point offset of  $145 \pm 8 \text{ km s}^{-1}$  to the FOS wavelength scale (see Appendix A for more details).

kinematics of this velocity component.

One drawback to our H I 21-cm, optical, and NUV spectra of PKS 1327–206 is that we are only sensitive to neutral or singly-ionized species at the redshift of ESO 1327–2041. We are therefore unable to speculate on the multi-phase nature of the absorbing gas, which may be crucial for understanding the radiation field incident on the 5255 and 5510  $\text{km s}^{-1}$  absorbers and thus their locations with respect to ESO 1327–2041. Detailed study of the ionization state of the absorbing gas requires searching for Lyman series H I lines or abundant metals of varying ionization states (e.g., C II, C III, C IV, Si II, Si III, Si IV, N V, O VI) in the far-UV (FUV) spectrum of PKS 1327–206 as has been done for other close QSO/galaxy pairs (see, e.g., Stocke et al. 2004; Keeney et al. 2005, 2006).

Unfortunately, there is a LLS at  $z = 0.85238$  that makes PKS 1327–206 too faint for FUV spectroscopy (see Appendix A and Bergeron et al. 1987). PKS 1327–206 was observed by the Galaxy Evolution Explorer (GALEX) as part of its All-Sky Imaging Survey and found to have a FUV magnitude of 21.2 ( $F_\lambda \approx 1.5 \times 10^{-16} \text{ ergs s}^{-1} \text{ cm}^{-2} \text{ \AA}^{-1}$ ). However, even with the exquisite FUV sensitivity of the recently-installed Cosmic Origins Spectrograph on *HST* (Green et al. 2010; Osterman et al. 2010) it would still take  $\sim 60$  orbits to reach  $S/N = 10$  per resolution element ( $\mathcal{R} \approx 18,000$ ) with the G160M grating ( $\lambda \approx 1400\text{--}1800 \text{ \AA}$ ), which covers the Si IV and C IV transitions.

Two recent papers (Gupta et al. 2010; Borthakur et al. 2010) have searched for H I 21-cm absorption in quasar-galaxy pairs culled from the Sloan Digital Sky Survey (SDSS). Both papers highlight the difficulty of detecting galaxies via H I 21-cm absorption: only 1 of 5 galaxies were detected by Gupta et al. (2010) and 1 of 12 by Borthakur et al. (2010), and both of these galaxies had impact parameters of  $\leq 11 h_{70}^{-1} \text{ kpc}$  to the quasar sight line. As for the PKS 1327–206 absorbers, Gupta et al. (2010) and Borthakur et al. (2010) found that their absorbers had DLA/sub-DLA column densities and were most likely associated with disk gas in the foreground galaxies. The Gupta et al. (2010) absorber has a significantly larger  $\mathcal{W}_\lambda(\text{Ca II})/\mathcal{W}_\lambda(\text{Na I})$  ratio ( $1.19 \pm 0.19$ ) than our PKS 1327–206 absorbers, however, which suggests that it is embedded in a stronger radiation field.

#### 4. DETECTION OF AN EJECTED GALAXY NUCLEUS?

There are several potential identifications for the compact object embedded in the stellar stream of ESO 1327–2041. The simplest explanation would be that it is a background elliptical galaxy projected in the middle of the stream by chance. However, our optical spectrum of this source (Fig. 3) shows that its radial velocity is  $5370 \pm 50 \text{ km s}^{-1}$ ,  $90 \pm 55 \text{ km s}^{-1}$  less than the absorption-line velocity of the lenticular nucleus to the south (see Tables 2 & 4), so it is clearly not a background object.

Another explanation would be that the compact object is a globular cluster. Close examination of the embedded source in Figure 1 shows that it has a relatively bright core surrounded by a more extended spheroid of lower surface brightness material. The core is marginally resolved with a FWHM of  $\sim 0''.2$  ( $70 h_{70}^{-1} \text{ pc}$ ) in our *HST* images, which is  $\sim 3$  times larger than  $\omega \text{ Cen}$ , the largest

globular cluster in the Milky Way (Tolstoy, Hill, & Tosi 2009). Furthermore, the core of the embedded object has an absolute B-band magnitude of  $M_B \approx -11.9$ , corresponding to a luminosity of  $L_B \approx 10^7 L_\odot$ , which is  $\sim 5$  times larger than typical globular cluster values ( $M_B \gtrsim -10$ ; Tolstoy et al. 2009). The more extended emission has a FWHM of  $\approx 2''$  ( $700 h_{70}^{-1} \text{ pc}$ ) and is  $\sim 3.5$  times brighter than the core of the embedded source. This measurement is somewhat uncertain, however, due to the presence of the stellar stream in which it is embedded.

Tidal streams created by tidal disruption of a dwarf companion galaxy have been identified in the halo of our Galaxy (Mathewson, Cleary, & Murray 1974; Majewski et al. 2003; Newberg et al. 2003; Yanny et al. 2003; Rocha-Pinto et al. 2003) and in a few other nearby galaxies (e.g., M 31; Ibata et al. 2001; Ferguson et al. 2002; Guhathakurta et al. 2006; Brown et al. 2006). If both the compact source and the stellar stream of ESO 1327–2041 were originally parts of a dwarf companion, it would have had  $M_B \lesssim -16.0$  ( $L_B \gtrsim 4 \times 10^8 L_\odot$ ). Grant, Kuipers, & Phillipps (2005) found that  $\gtrsim 80\%$  of dwarf ellipticals in the Virgo cluster with  $M_B \leq -16$  had central nuclei. Further, the two closest examples of nucleated dwarfs, the M 31 satellites M 32 and NGC 205, both show strong Balmer absorption in their nuclei (Ho, Filippenko, & Sargent 1995) similar to the Balmer absorption seen in the compact object (see Fig. 3). Recent ground-based spectroscopy of dwarf ellipticals in the Fornax cluster and nearby galaxy groups (Koleva et al. 2009) have also found evidence for gradients in age (increasing) and metallicity (decreasing) with increasing galaxy radius, which would explain the age differences between the compact object and the stellar stream (see §2.4). Given these compelling similarities we cannot be conclusive about ruling out a tidally-disrupted dwarf galaxy producing this stream and nucleus, but arguments against this hypothesis include: (1) This scenario requires a collision between three galaxies, not two, a much rarer occurrence; and (2) this explanation does not account for the absence of a second nucleus in the two galaxies to the south.

Instead, we propose that the hyper-compact object in the stellar stream is the spiral’s nucleus, ejected during the collision. Given that the nucleus has an early-to-mid A star spectrum, as evidenced by strong Balmer absorption with no associated emission, an age for these stars is estimated to be  $\sim 1 \text{ Gyr}$ . If this age indicates the time of a starburst created by the collision, then there is plenty of time for the nucleus to reach its current location  $14 h_{70}^{-1} \text{ kpc}$  in projection from the center of the spiral arms to the south and consistent with the (poorly constrained) radial velocity difference of  $90 \pm 55 \text{ km s}^{-1}$  between the ejected nucleus and the lenticular nucleus. The somewhat older stars in the stellar stream would constitute a small bulge of pre-existing stars also ejected during the collision, some with larger and some with smaller ejection velocities than the ejected nucleus. However, the spiral would also have had time to move a comparable or larger distance on the sky since this putative merger-triggered starburst. So, by the ejected nucleus hypothesis, it appears likely that the current collision is not the first close passage of these two galaxies and we are seeing

these galaxies during their second or third close passage.

Alternatively, the age of the nuclear star cluster may not be related to the galaxy-galaxy collision, in which case the nucleus could have been ejected at a significantly higher velocity given the lack of proper motion between the lenticular and the spiral structure superposed on it; i.e., the collision which ejected the nucleus is very much still on-going. The poor constraint on the velocity difference mentioned above and the unknown inclination angle of the ejected nucleus' path allow for a consistent picture but do not constrain this picture significantly. So, the required scenario for an ejected spiral nucleus is somewhat complicated. This unresolved discussion invites a numerical simulation to determine how easily these observables can be reproduced (e.g., Barnes & Hibbard 2009) and would lend considerable credence to the ejected nucleus hypothesis if they are reproducible.

Current simulations predict that there are two scenarios which can lead to the ejection of a galaxy nucleus as a result of the interaction of two galaxies: grazing-incidence tidal interactions and mergers (e.g., Moore et al. 1996; Komossa & Merritt 2008a,b). In both scenarios, the ejected nucleus is expected to consist of a supermassive black hole surrounded by a compact stellar system with a radius of a few tens of parsecs. In the case of galaxy mergers, one of the nuclei can receive a kick of up to  $\sim 1000 \text{ km s}^{-1}$  from asymmetric gravitational wave emission associated with the merger, causing the displaced black hole and any stars within its gravitational sphere of influence to be ejected from the host galaxy (Komossa & Merritt 2008a,b). Usually the so-called hypercompact galaxy nucleus that is ejected remains bound to the new system and eventually sinks via dynamical friction to its center where it will merge with the undisplaced nucleus. The predictions of these simulations agree very well with what we observe in ESO 1327–2041.

While we do not know of a completely conclusive test of the ejected nucleus hypothesis, the detection of a weak AGN in this hyper-compact object would argue strongly in favor of that hypothesis. Our VLA L-band continuum images set a  $3\sigma$  flux limit of  $\lesssim 1 \text{ mJy}$  (corresponding to  $L \lesssim 10^{21} \text{ W Hz}^{-1}$ ) at the position of this knot. Since many elliptical galaxies have weak radio sources less luminous than this (Nagar et al. 2002) this limit is not conclusive, especially in the context of an ejected spiral nucleus, which would normally be radio-quiet.

Loeb (2007) has assessed the circumstances by which a supermassive black hole and at least a portion of its accretion disk could be ejected from a galaxy merger in progress. He finds that the disk accretion could survive for a few million years allowing the black hole to move  $\sim 10 \text{ kpc}$  away from the galaxy nucleus. Since this is the approximate distance that the candidate ejected nucleus identified here is from its putative nuclear location, there is some chance that it may be still accreting. A moderately deep *Chandra* image might detect an X-ray source associated with a weak AGN in this nucleus and is likely the best observational test; i.e., an  $\sim 10^7 M_{\odot}$  black hole accreting at  $\sim 1\%$  of the Eddington rate would be detectable with *Chandra* in a few tens of ksecs.

Recently, Comerford et al. (2009a,b) have proposed other candidate ejected nuclei based upon a large ra-

dial velocity difference between two emission line components in a distant AGN (see also Boroson & Lauer 2009). However, given the large cosmological distance to these ejected nuclei candidates, little detail can be discerned to confirm their hypothesis.

## 5. CONCLUSIONS

In this paper we have presented new *HST* imaging and supporting ground-based imaging and spectroscopy of the complex galaxy system ESO 1327–2041, which is located near on the sky to the background quasar PKS 1327–206, whose optical, UV, and radio spectra contain absorption lines due to the foreground galaxy. The *HST* images reveal that a spiral galaxy is in the process of colliding with a lenticular galaxy since different nebular regions in the spiral arms are seen in front of or behind the lenticular's bulge. Ground-based imaging and spectroscopy confirms that these nebular regions are H II regions with velocities close to that of the lenticular's nucleus. Thus, there is no doubt that these two systems are co-spatial (see Fig. 1). The rather diffuse H I 21-cm emission associated with this system confirms this conclusion since, while some H I is associated with the spiral arms in the late-type galaxy disk, much of it has been ejected from the spiral and is detected far to the north and east of the optical galaxy. There may also be some diffuse H I to the south of these galaxies. However, the size of the H I emitting area of ESO 1327–2041 is not appreciably larger than our estimates of the pre-merger size of the galaxy (see Fig. 2).

The *HST* and ground-based images also detect a “stellar stream” extending parallel to the H I stream to the north, which we identify as a tidal feature also created in the collision. Unique to this tidal feature (to our knowledge) the *HST* images have discovered a marginally resolved source centered in the stream with an intermediate age ( $\sim 1 \text{ Gyr}$ ) stellar population. This knot is too luminous ( $\sim 10^7 L_{\odot}$ ) and too large to be a globular cluster and is unlikely to be the nucleus of a tidally-disrupted dwarf companion to these galaxies. We suggest that this knot is the hypercompact galaxy nucleus of the inclined spiral component of ESO 1327–2041, which was ejected from the system as a result of its recent interaction with the lenticular component and is itself being shredded by tides to produce the observed stellar stream. This assertion can be supported by detecting a non-thermal X-ray point source associated with the putative ejected nucleus and by numerical modeling of an early-type/late-type galaxy merger that results in the formation of a polar ring galaxy (Whitmore et al. 1990; Barnes & Hibbard 2009).

The PKS 1327–206 / ESO 1327–2041 system provides us with a very detailed, and far from simple, view of a DLA/sub-DLA system. Rather than an isolated gaseous disk of H I, this DLA/sub-DLA is a mixture of two components, only one of which appears related to the spiral disk. However, both have Ca II / Na I ratios typical of the disk of the Milky Way and not of halo gas. In fact, the narrow high-velocity component has a smaller Ca II / Na I ratio than the broad H I component we have identified as due to the outer spiral arm and so we also identify this as disk, not halo or HVC, material. Following CvG92, the best identification of the  $\sim 5250 \text{ km s}^{-1}$  component appears to be with the diffuse tidally-disrupted H I found by those authors to the northeast of ESO 1327–



2041 at similar velocities.

Using a spin temperature of 100 K, appropriate for galactic disk material, the column density associated with the outer spiral arm at  $\sim 5500 \text{ km s}^{-1}$  and the column density associated with the high velocity component at  $\sim 5250 \text{ km s}^{-1}$  are nearly equal and, if added together, yield a total  $\log N_{\text{HI}} \approx 19.8 \text{ cm}^{-2}$ , a sub-DLA (see § 3.1). However, using these estimated column densities and the velocity separation for the two components, we have simulated the Ly $\alpha$  profile of this entire system and find it to be best-fit by a sub-DLA with  $\log N_{\text{HI}} = 20.0$  when the signal-to-noise of the spectrum is modest ( $\lesssim 15$ ) and the presence of a dense Ly $\alpha$  forest makes the wings of the sub-DLA profile more uncertain (as would be present at higher redshifts). We suggest that using a single-component Ly $\alpha$  profile to determine  $N_{\text{HI}}$  for DLAs and sub-DLAs with multiple metal-line components (i.e., the gas associated with the DLA/sub-DLA has at least two velocity components) overpredicts the total H I column density of the system.

In summary, of the three low- $z$  QSO/galaxy pairs with likely DLA or sub-DLA absorbers that we have imaged using *HST*, neither 3C 232 / NGC 3067 nor PKS 1327–206 / ESO 1327–2041 appear to have absorbers that are associated with quiescent thick disk gas. This is in keeping with a recent suggestion by Zwaan et al. (2008) that the widths of low-ionization metal lines are too broad by a factor of two to be consistent with the canonical model of DLAs arising due to ordered rotation in cold disks (Wolfe et al. 1986, 1995; Lanzetta et al. 1991). Zwaan et al. (2008) conclude that superwind outflows or galaxy interactions are most likely the cause of the broader velocity widths. The current observational work supports this conclusion, particularly the case presented here.

However, we do note that the third QSO/galaxy pair in our study, PKS 2020–370 / Klemola 31A does appear consistent with rotating disk gas. CvG92 show that the

observed H I 21-cm emission contour at the quasar location is  $\sim 2 \times 10^{20} \text{ cm}^{-2}$  with velocities consistent with disk rotation. Our *HST* images show no H $\alpha$  emission beyond the spiral arms in Klemola 31A and neither line nor continuum emission is observed at the quasar location. If we imagine that our small sample of H I 21-cm and Ca II / Na I absorption-selected DLA/sub-DLAs are representative, then we expect that other DLA samples are a rather uniform mixture of disk gas, halo gas, and gas whose cross-section on the sky has been modestly increased by tidal interactions during galaxy collisions and mergers.

B. A. K., J. T. S., and C. W. D. gratefully acknowledge support from NASA *HST* General Observer grant GO-10925, as well as NASA grant NNX08AC14G. C. L. C. thanks the Max-Planck-Gesellschaft and the Humboldt-Stiftung for support through the Max-Planck-Forschungspreis. We would also like to thank J. Darling for many useful discussions as this work progressed.

This work is based on observations made with the NASA/ESA *HST*, the Apache Point Observatory 3.5-m telescope, and the Very Large Array of the National Radio Astronomy Observatory (NRAO). The *HST* data were obtained at the Space Telescope Science Institute, which is operated by the Association of Universities for Research in Astronomy, Inc., under NASA contract NAS5-26555. The Apache Point Observatory 3.5-m telescope is owned and operated by the Astrophysical Research Consortium. The NRAO is a facility of the National Science Foundation operated under cooperative agreement by Associated Universities, Inc. This research has also made use of the NASA/IPAC Extragalactic Database, which is operated by the Jet Propulsion Laboratory, California Institute of Technology, under contract with the National Aeronautics and Space Administration.

## APPENDIX

### OTHER ABSORBERS IN THE NEAR-UV SPECTRUM OF PKS 1327–206

The *HST*/FOS spectrum of PKS 1327–206 is filled with absorption lines from a variety of redshifts, including lines associated with ESO 1327–2041 at  $z = 0.0178$  ( $cz \approx 5500 \text{ km s}^{-1}$ ; see § 3.3), lines associated with the LLS at  $z = 0.85238$  (Bergeron et al. 1987), intergalactic Ly $\alpha$  forest absorbers, and Galactic ISM absorbers. Here we present measurements of the absorption-line parameters of these systems. Figure 7 displays the full FOS spectrum of PKS 1327–206 with quasar emission lines at  $z = 1.169$  labelled. The dashed vertical lines indicate the positions of absorption lines associated with ESO 1327–2041 (see § 3.3, Fig. 6, and Table 7).

Table 8 lists the line identification, rest wavelength, observed wavelength, heliocentric velocity, and rest-frame equivalent width of all Galactic ISM absorbers detected at  $> 4\sigma$  confidence. We detect ISM absorption from four Fe II transitions, two Mn II lines, the Mg II  $\lambda\lambda 2796, 2804$  doublet, and Mg I  $\lambda 2853$ . We have added a zero-point offset of  $145 \pm 8 \text{ km s}^{-1}$  to the FOS wavelength scale so that the interstellar absorption lines have an average velocity (excluding Mn II  $\lambda 2594$ ) of  $v_{\text{helio}} = 0 \pm 10 \text{ km s}^{-1}$ . This same zero-point offset has been added to all wavelengths, velocities, and redshifts in Tables 7–10.

The LLS is clearly detected in a number of neutral to moderately-ionized species. Table 9 lists the line identification, rest wavelength, observed wavelength, redshift, and rest-frame equivalent width of all lines detected at  $> 4\sigma$  confidence (observed  $\mathcal{W}_\lambda > 200 \text{ m}\text{\AA}$ ) that are associated with the LLS. The average redshift of these absorption lines is  $z = 0.85238 \pm 0.00001$ . Figure 8 shows the absorption line profiles of all lines listed in Table 9.

Finally, Table 10 lists the line identification, rest wavelength, observed wavelength, redshift, and rest-frame equivalent width for all IGM absorbers detected at  $> 4\sigma$  confidence. Fourteen Ly $\alpha$  absorbers are detected at redshifts ranging from 0.84579 to 1.13536. We also detect one C IV  $\lambda 1548$  absorber at  $z = 0.85021$  that lies  $780 \pm 20 \text{ km s}^{-1}$  blueward of the C IV  $\lambda\lambda 1548, 1551$  absorbers associated with the LLS. The C IV  $\lambda 1551$  absorption at  $z = 0.85021$  is blended with the C IV  $\lambda 1548$  absorption from the LLS, and the corresponding Ly $\alpha$  absorber is blended with the LLS Ly $\alpha$ . While

this absorber may represent a blue component to the LLS absorption, it is not present in any of the LLS absorption profiles in Figure 8 except for C IV.

## REFERENCES

- Adelberger, K. L., Steidel, C. C., Shapley, A. E., & Pettini, M. 2003, *ApJ*, 584, 45
- Anderson, L. D., Bania, T. M., Jackson, J. M., Clemens, D. P., Heyer, M., Simon, R., Shah, R. Y., & Rathborne, J. M. 2009, *ApJS*, 181, 255
- Barnes, J. E. & Hibbard, J. E. 2009, *AJ*, 137, 3071
- Bergeron, J., Kunth, D., & D'Odorico, S. 1987, *A&A*, 180, 1
- Boksenberg, A. & Sargent, W. L. W. 1978, *ApJ*, 220, 42
- Boroson, T. A. & Lauer, T. R. 2009, *Nature*, 458, 53
- Borthakur, S., Tripp, T. M., Yun, M. S., Bowen, D. V., Meiring, J. D., York, D. G., & Momjian, E. M. 2010, *ApJ*, submitted (astro-ph/1007.3936)
- Bournaud, F. & Combes, F. 2003, *A&A*, 401, 817
- Broeils, A. H. & Rhee, M.-H. 1997, *A&A*, 324, 877
- Brown, T. M., Smith, E., Ferguson, H. C., Rich, R. M., Guhathakurta, P., Renzini, A., Sweigart, A. V., & Kimble, R. A. 2006, *ApJ*, 652, 323
- Carilli, C. L. & van Gorkom, J. H. 1992, *ApJ*, 399, 373 (CvG92)
- Churchill, C. W., Kacprzak, G. G., Steidel, C. C., & Evans, J. L. 2007, *ApJ*, 661, 714
- Comerford, J. M. et al. 2009a, *ApJ*, 698, 956
- Comerford, J. M., Griffith, R. L., Gerke, B. F., Cooper, M. C., Newman, J. A., Davis, M., & Stern, D. 2009b, *ApJ*, 702, L82
- Ferguson, A. M. N., Irwin, M. J., Ibata, R. A., Lewis, G. F., & Tanvir, N. R. 2002, *AJ*, 124, 1452
- Giraud, E. 1986, *A&A*, 161, 206
- Grant, N. I., Kuipers, J. A., & Phillipps, S. 2005, *MNRAS*, 363, 1019
- Green, J. C. et al. 2010, *ApJ*, in prep.
- Guyathakurta, P., et al. 2006, *AJ*, 131, 2497
- Gupta, N., Srianand, R., Bowen, D. V., York, D. G., & Wadadekar, Y. 2010, *MNRAS*, in press (astro-ph/1007.0288)
- Haynes, M. P. & Giovanelli, R. 1984, *AJ*, 89, 758
- Heckman, T. M., Sembach, K. R., Meurer, G. R., Leitherer, C., Calzetti, D., & Martin, C. L. 2001, *ApJ*, 558, 56
- Ho, L. C., Filippenko, A. V., & Sargent, W. L. W. 1995, *ApJS*, 98, 477
- Ibata, R., Irwin, M., Lewis, G., Ferguson, A. M. N., & Tanvir, N. 2001, *Nature*, 412, 49
- Kacprzak, G. G., Churchill, C. W., Ceverino, D., Steidel, C. C., Klypin, A., & Murphy, M. T. 2010, *ApJ*, 711, 533
- Keeney, B. A., Momjian, E., Stocke, J. T., Carilli, C. L., & Tumlinson, J. 2005, *ApJ*, 622, 267
- Keeney, B. A., Stocke, J. T., Rosenberg, J. L., Tumlinson, J., & York, D. G. 2006, *AJ*, 132, 2496
- Kennicutt, R. C., Jr. 1998, *ARA&A*, 36, 189
- Kennicutt, R. C., Jr., Lee, J. C., Funes, J. G., Sakai, S., & Akiyama, S. 2008, *ApJS*, 178, 247
- Kereš, D. & Hernquist, L. 2009, *ApJ*, 700, L1
- Koleva, M., De Rijcke, S., Prugniel, P., Zailing, W. W., & Michielsen, D. 2009, *MNRAS*, 396, 2133
- Komossa, S. & Merritt, D. 2008a, *ApJ*, 683, L21
- Komossa, S. & Merritt, D. 2008b, *ApJ*, 689, L89
- Kunth, D. & Bergeron, J. 1984, *MNRAS*, 210, 873
- Lanzetta, K. M., McMahon, R. G., Wolfe, A. M., Turnshek, D. A., Hazard, C., & Lu, L. 1991, *ApJS*, 77, 1
- Loeb, A. 2007, *Phys. Rev. Lett.*, 99, 041103
- Majewski, S. R., Skrutskie, M. F., Weinberg, M. D., & Ostheimer, J. C. 2003, *ApJ*, 599, 1082
- Martin, C. L. 1999, *ApJ*, 513, 156
- Mathewson, D. S., Cleary, M. N., & Murray, J. D. 1974, *ApJ*, 190, 291
- Mo, H. J. & Miralda-Escude, J. 1996, *ApJ*, 469, 589
- Moiseev, A. V. & Bizyaev, D. V. 2009, *New Astronomy Reviews*, 53, 169
- Moore, B., Katz, N., Lake, G., Dressler, A. & Oemler, A. 1996, *Nature*, 379, 613
- Morton, D. C. & Blades, J. C. 1986, *MNRAS*, 220, 927
- Nagar, N. M., Falcke, H., Wilson, A. S., & Ho, L. C. 2002, *New A Rev.*, 46, 225
- Nestor, D. B., Turnshek, D. A., & Rao, S. M. 2005, *ApJ*, 628, 637
- Nestor, D. B., Turnshek, D. A., & Rao, S. M. 2006, *ApJ*, 643, 75
- Newberg, H. J., et al. 2003, *ApJ*, 596, L191
- Noordermeer, E., van der Hulst, J. M., Sancisi, R., Swaters, R. A., & van Albada, T. S. 2005, *A&A*, 442, 137
- Osterman, S., et al. 2010, *ApJ*, in prep.
- Prochaska, J. X. & Herbert-Fort, S. 2004, *PASP*, 116, 622
- Rao, S. M., Turnshek, D. A., & Nestor, D. B. 2006, *ApJ*, 636, 610
- Richter, P., Charlton, J. C., Fangano, A. P. M., Bekhti, N. B., & Masiero, J. R. 2009, *ApJ*, 695, 1631
- Rocha-Pinto, H. J., Majewski, S. R., Skrutskie, M. F., & Crane, J. D. 2003, *ApJ*, 594, L115
- Rosenberg, J. L. & Schneider, S. E. 2003, *ApJ*, 585, 256
- Roy, N., Chengalur, J. N., & Srianand, R. 2006, *MNRAS*, 365, L1
- Sembach, K. R. & Savage, B. D. 1992, *ApJS*, 83, 147
- Steidel, C. C. 1995, in *QSO Absorption Lines*, ed. G. Meylan (Garching: Springer), 139
- Stocke, J. T., Case, J., Donahue, M., Shull, J. M., & Snow, T. P. 1991, *ApJ*, 374, 72
- Stocke, J. T., Keeney, B. A., McLin, K. M., Rosenberg, J. L., Weymann, R. J., & Giroux, M. L. 2004, *ApJ*, 609, 94
- Stocke, J. T., Keeney, B. A., & Danforth, C. W. 2010, *PASA*, 27, 256
- Tolstoy, E., Hill, V., & Tosi, M. 2009, *ARA&A*, 47, 371
- Whitmore, B. C., Lucas, R. A., McElroy, D. B., Steiman-Cameron, T. Y., Sackett, P. D., & Olling, R. P. 1990, *AJ*, 100, 1489
- Wolfe, A. M., Turnshek, D. A., Smith, H. E., & Cohen, R. D. 1986, *ApJS*, 61, 249
- Wolfe, A. M., Lanzetta, K. M., Foltz, C. B., & Chaffee, F. H. 1995, *ApJ*, 454, 698
- Wolfe, A. M. & Prochaska, J. X. 2000a, *ApJ*, 545, 603
- Wolfe, A. M., Gawiser, E., & Prochaska, J. X. 2005, *ARA&A*, 43, 861
- Yanny, B., et al. 2003, *ApJ*, 588, 824
- York, D. G., Dopita, M., Green, R., & Bechtold, J. 1986, *ApJ*, 311, 610

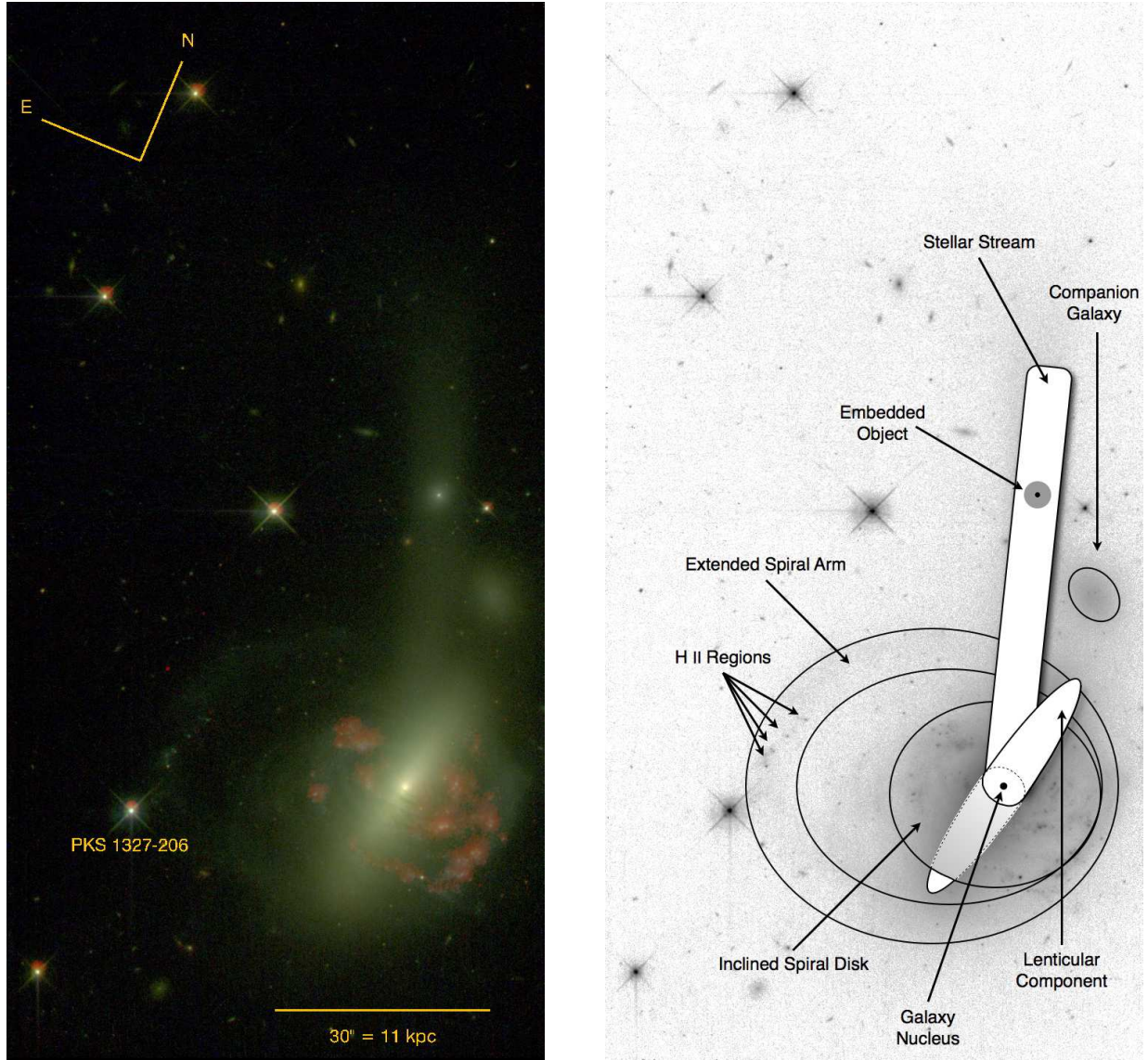


**Figure 1.** *Left:* Color composite *HST*/WFPC2 image of ESO 1327–2041. Data from the F450W filter is displayed in blue, F675W in green, and F791W in red. The image orientation and the location of the nearby quasar PKS 1327–206 are labelled. The lower resolution red regions near the center of the galaxy are H II regions found in our ground-based H $\alpha$  images (§ 2.2). The field-of-view of the image is approximately  $75'' \times 150''$ , which corresponds to a physical scale of  $\sim 28 \times 56 h_{70}^{-1}$  kpc at the galaxy redshift. *Right:* Schematic diagram of ESO 1327–2041 overlaid on the F675W WFPC2 image. All galaxy components discussed in § 2 have been labelled.

**Table 1**  
H I 21-cm Emission Properties of ESO 1327–2041

Region <sup>a</sup>	RA (J2000.0)	Dec (J2000.0)	$v_{\text{peak}}^{\text{b}}$ (km s <sup>-1</sup> )	$M_{\text{HI}}$ ( $10^8 h_{70}^{-2} M_{\odot}$ )
A	13 30 05.2	-20 55 56	5338	$2.61 \pm 0.33$
B	13 30 06.7	-20 55 49	5402	$1.81 \pm 0.23$
C	13 30 06.4	-20 56 18	5306	$1.91 \pm 0.25$
D	13 30 07.7	-20 55 18	5263	$1.01 \pm 0.13$
E	13 30 07.6	-20 54 38	5253	$2.22 \pm 0.28$

<sup>a</sup> Region of interest as indicated in Fig. 2.

<sup>b</sup> The channel velocity of the H I 21-cm emission peak for this region.

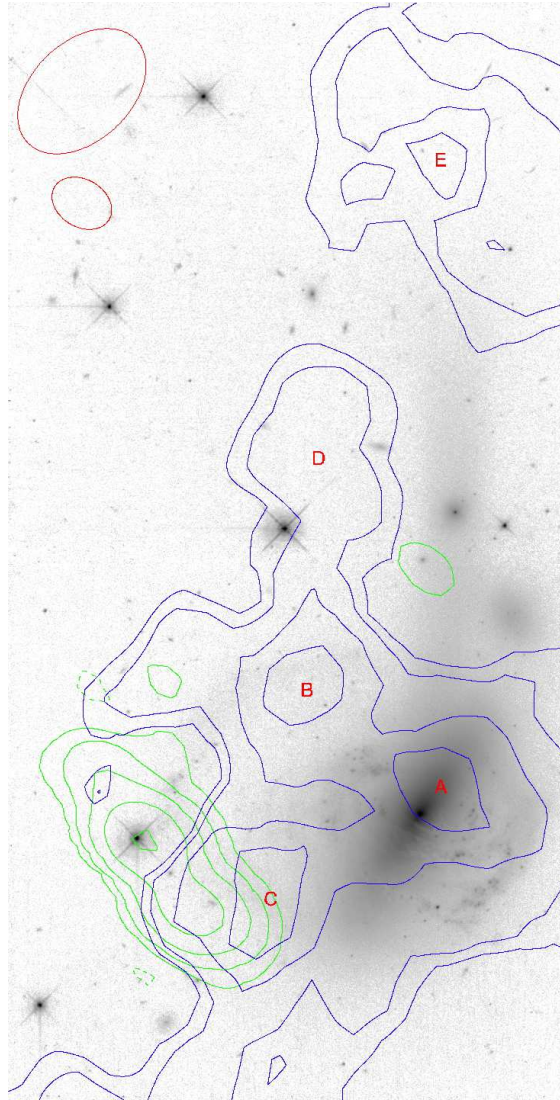


**Figure 2.** Natural-weighted H I 21-cm emission contours for ESO 1327–2041 (*blue*) and uniform-weighted L-band continuum contours for PKS 1327–206 (*green*) overlaid on our F675W WFPC2 data. The H I contour levels are  $2.5, 5, 10,$  and  $15 \times 10^{20}$  atoms  $\text{cm}^{-2}$  and the continuum contour levels are  $-3, 3, 9, 27, 81,$  and  $243$  mJy  $\text{beam}^{-1}$ . The large red ellipse ( $20'' \times 13''$ ) in the upper-left corner of the image is the restoring beam for the H I contours; the smaller ellipse ( $9'' \times 6''$ ) is the restoring beam for the continuum contours, and the labelled regions (A–E) correspond to the regions in Table 1.

**Table 2**  
Absorption Lines Detected in the Embedded Source

ID	$\lambda_{\text{rest}}$ (Å)	$\lambda_{\text{obs}}$ (Å)	$v_{\text{helio}}$ ( $\text{km s}^{-1}$ )	$W_{\lambda}$ (Å)
H $\eta$	3835.38	$3900.2 \pm 2.4$	$5090 \pm 190$	$13.7 \pm 9.7$
H $\zeta$	3889.05	$3957.4 \pm 3.7$	$5290 \pm 290$	$7.8 \pm 6.7$
Ca II K	3933.66	$4005.2 \pm 1.4$	$5480 \pm 110$	$3.3 \pm 2.3$
He <sup>a</sup>	3970.07	$4040.1 \pm 3.9$	$5310 \pm 300$	$15.4 \pm 8.9$
H $\delta$	4101.73	$4172.5 \pm 2.6$	$5190 \pm 190$	$9.0 \pm 2.7$
H $\gamma$	4340.46	$4416.7 \pm 2.9$	$5290 \pm 200$	$9.3 \pm 3.5$
H $\beta$	4861.32	$4946.4 \pm 2.2$	$5270 \pm 140$	$7.4 \pm 2.4$
Na I D	5891.94	$5995.6 \pm 4.8$	$5300 \pm 250$	$3.2 \pm 1.5$
H $\alpha$	6562.80	$6683.2 \pm 2.3$	$5520 \pm 110$	$3.7 \pm 1.0$

**Note.** — The average absorption-line velocity for this source is  $5370 \pm 50$   $\text{km s}^{-1}$ .

<sup>a</sup> This line is blended with Ca II H but we attribute most of the absorption to He given the presence of higher-order Balmer absorption in this spectrum.

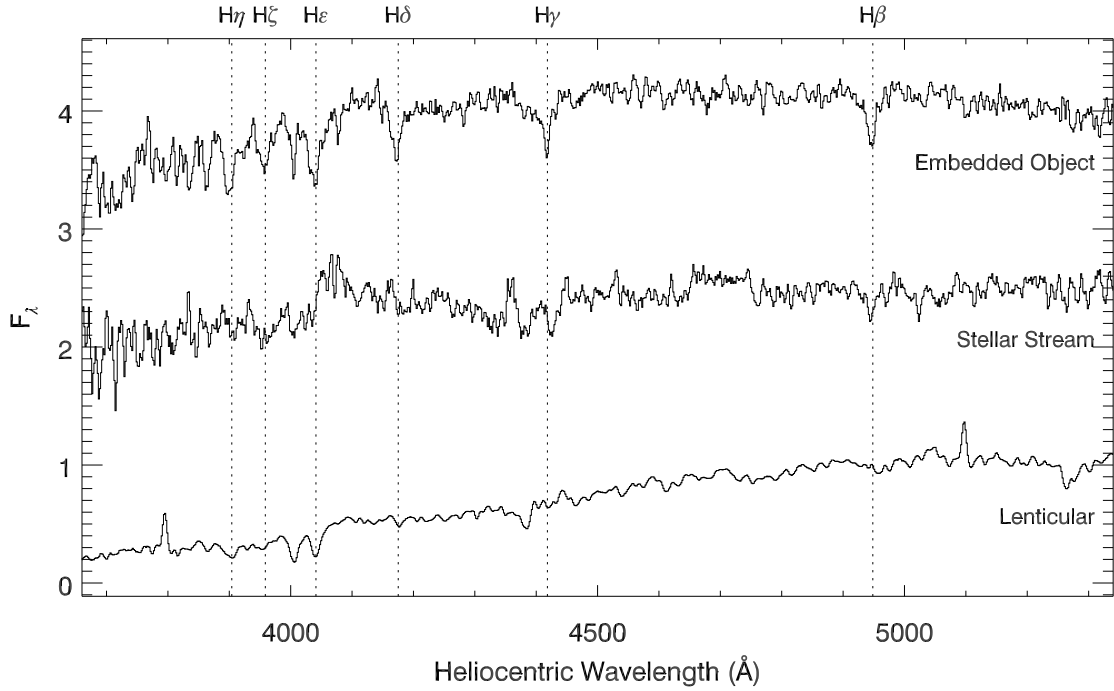


**Figure 3.** The blue portion of our optical spectra of the lenticular region of ESO 1327–2041 (*bottom*), the stellar stream of material (*middle*), and the compact object embedded within the stream (*top*). The vertical axis is displayed in arbitrarily-scaled  $F_\lambda$  units. The dashed vertical lines indicate the positions of the  $H\beta$ – $H\eta$  absorption lines detected in the embedded source at  $cz = 5370 \pm 50 \text{ km s}^{-1}$ . The lenticular spectrum also contains [O II]  $\lambda 3717$  and [O III]  $\lambda 5007$  emission from a foreground H II region in the slit (see Table 4).

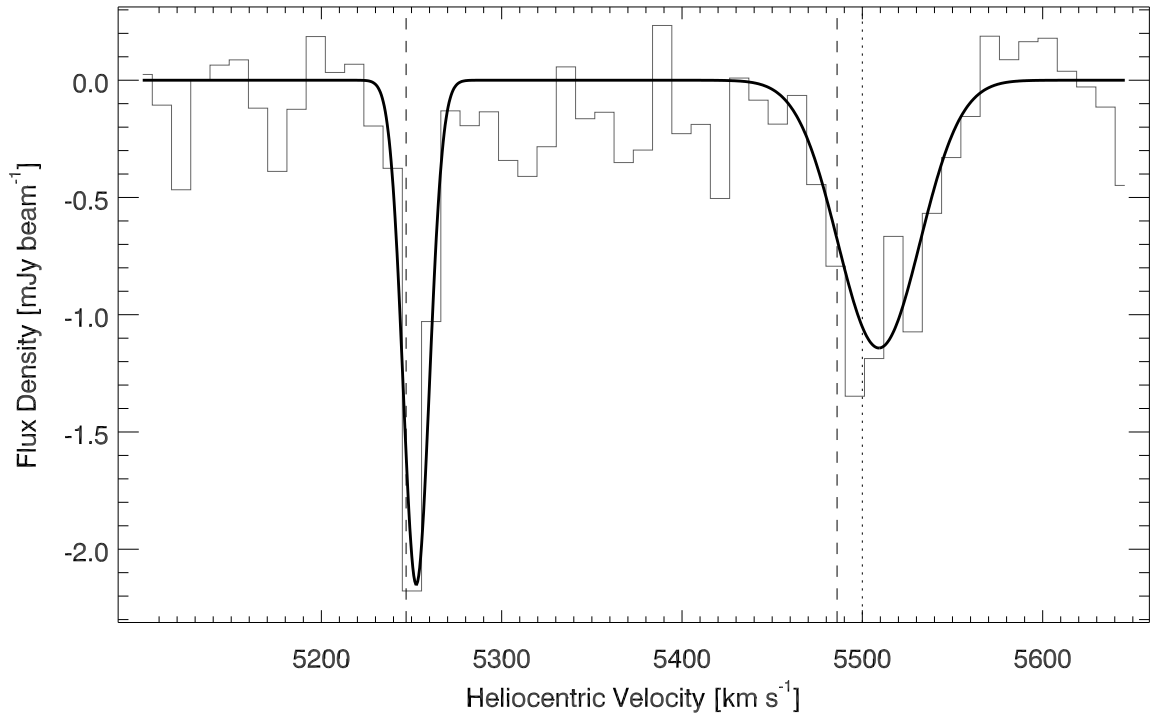


**Figure 4.** The H I 21-cm absorption spectrum of PKS 1327–206 at  $20'' \times 13''$  resolution and  $10.4 \text{ km s}^{-1} \text{ channel}^{-1}$  with best-fit absorption line profiles (see Table 5) overlaid. The dashed vertical lines show the velocities of the Na I D absorption components found by Bergeron et al. (1987). The dotted vertical line indicates the disk velocity at the position of PKS 1327–206, extrapolated from H II regions in the extended spiral arm of ESO 1327–2041 (see § 2.4).

**Table 3**  
Absorption Lines Detected in the Stellar Stream

ID	$\lambda_{\text{rest}}$ (Å)	$\lambda_{\text{obs}}$ (Å)	$v_{\text{helio}}$ (km s <sup>-1</sup> )	$\mathcal{W}_\lambda$ (Å)
Ca II K	3933.66	4006.8 ± 3.9	5600 ± 300	3.8 ± 2.4
Ca II H	3968.47	4036.7 ± 2.6	5180 ± 190	3.3 ± 1.7
G-band	4304.40	4382.4 ± 2.2	5460 ± 160	4.7 ± 3.6
H $\gamma$	4340.46	4425.7 ± 1.9	5910 ± 130	5.9 ± 3.7
H $\beta$	4861.32	4945.9 ± 5.2	5240 ± 320	4.8 ± 2.4

**Note.** — The average absorption-line velocity for this source is 5590 ± 80 km s<sup>-1</sup>.

**Table 4**  
Lines Detected in the Lenticular Nucleus

Emission Lines					Absorption Lines				
ID	$\lambda_{\text{rest}}$ (Å)	$\lambda_{\text{obs}}$ (Å)	$v_{\text{helio}}$ (km s <sup>-1</sup> )	Integ. Flux (10 <sup>-16</sup> ergs s <sup>-1</sup> cm <sup>-2</sup> )	ID	$\lambda_{\text{rest}}$ (Å)	$\lambda_{\text{obs}}$ (Å)	$v_{\text{helio}}$ (km s <sup>-1</sup> )	$\mathcal{W}_\lambda$ (Å)
[O II]	3727.42	3794.7 ± 0.5	5400 ± 40	9.4 ± 3.6	Ca II K	3933.66	4005.9 ± 0.6	5500 ± 50	10.3 ± 3.1
[O III]	5007.84	5096.9 ± 0.4	5330 ± 30	10.4 ± 2.4	Ca II H	3968.47	4041.1 ± 0.7	5480 ± 50	10.8 ± 3.0
[N II]	6548.04	6664.2 ± 1.2	5310 ± 60	3.3 ± 0.8	G-band	4304.40	4382.4 ± 1.0	5430 ± 70	6.6 ± 2.4
H $\alpha$	6562.80	6680.6 ± 0.3	5380 ± 20	15.1 ± 1.6	Na I D	5891.94	5999.2 ± 0.6	5450 ± 30	4.9 ± 0.7
[N II]	6583.46	6701.9 ± 0.3	5390 ± 20	14.6 ± 1.6					
[S II]	6716.44	6837.3 ± 1.0	5390 ± 40	5.7 ± 1.0					
[S II]	6730.82	6852.0 ± 0.8	5390 ± 40	6.1 ± 1.0					

**Note.** — The average emission-line velocity for this source is 5380 ± 10 km s<sup>-1</sup> and the average absorption-line velocity is 5460 ± 20 km s<sup>-1</sup>.

**Table 5**  
Gaussian Fits to H I 21 cm Absorbers Detected Toward  
PKS 1327-206

$v_{\text{helio}}$ (km s <sup>-1</sup> )	FWHM (km s <sup>-1</sup> )	$\tau_0$	$N_{\text{HI}}/(T_{\text{spin}}/f)$ (10 <sup>17</sup> cm <sup>-2</sup> K <sup>-1</sup> )
5255 ± 5	17 ± 7	0.0068 ± 0.0006	2.3 ± 1.0
5510 ± 10	54 ± 18	0.0042 ± 0.0006	4.3 ± 1.6

**Table 6**  
Lines Associated with ESO 1327-2041 in the Optical  
Spectrum of PKS 1327-206

ID	$\lambda_{\text{rest}}$ (Å)	$\lambda_{\text{obs}}$ (Å)	$v_{\text{helio}}$ (km s <sup>-1</sup> )	$\mathcal{W}_\lambda$ (mÅ)
Ca II K	3933.663	4002.7 ± 0.8	5260 ± 60	170 ± 140
		4005.5 ± 0.5	5470 ± 40	590 ± 190
Ca II H	3968.469	4038.1 ± 0.8	5260 ± 60	90 ± 80 <sup>a</sup>
		4040.9 ± 0.5	5470 ± 40	330 ± 110 <sup>a</sup>
Na I D2	5889.950	5992.9 ± 0.2	5240 ± 10	610 ± 80
		5997.7 ± 0.2	5480 ± 10	830 ± 90
Na I D1	5895.924	5998.9 ± 0.2	5240 ± 10	400 ± 70
		6003.8 ± 0.2	5480 ± 10	640 ± 80

<sup>a</sup> The equivalent widths for the Ca II H lines were calculated from the apparent column densities measured in the Ca II K line profiles, assuming optically thin absorption.

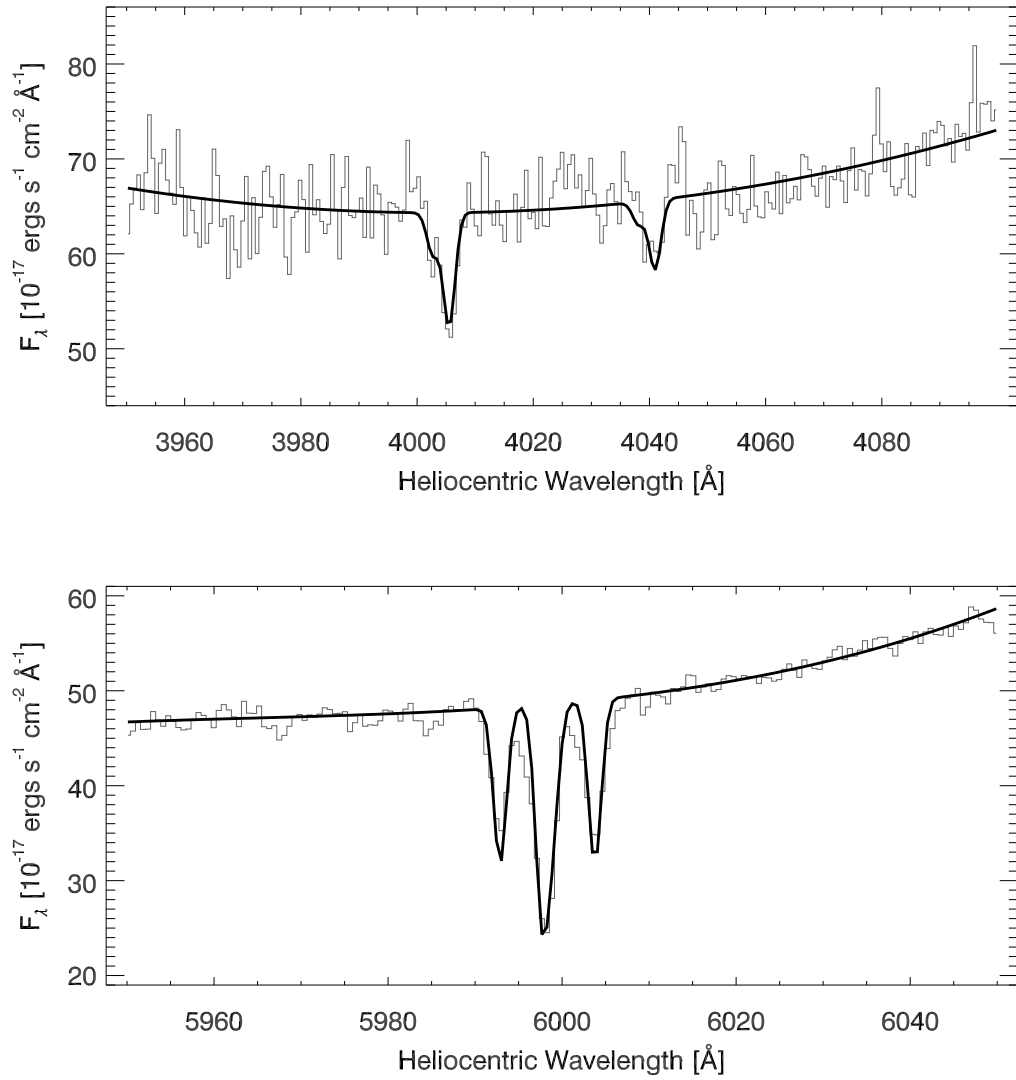


**Figure 5.** The regions surrounding the Ca II H & K (*top*) and Na I D (*bottom*) absorption lines associated with ESO 1327–2041 in the optical spectrum of PKS 1327–206, with best-fit absorption line profiles (see Table 6) overlaid.

**Table 7**  
Lines Associated with ESO 1327–2041 in the *HST*/FOS  
Spectrum of PKS 1327–206

ID	$\lambda_{\text{rest}}$ (Å)	$\lambda_{\text{obs}}$ (Å)	$v_{\text{helio}}$ (km s <sup>-1</sup> )	$\mathcal{W}_\lambda$ (mÅ)
Fe II	2344.21	2386.4 ± 0.2	5390 ± 30	1400 ± 170
Fe II	2382.77	2425.3 ± 0.2	5350 ± 20	2140 ± 100
Fe II	2586.65	2632.9 ± 0.2	5360 ± 20	1360 ± 140
Mn II	2594.50	2641.4 ± 0.2	5420 ± 20	1590 ± 180
Fe II	2600.17	2645.7 ± 0.2	5250 ± 20	3440 ± 160
Mg II	2796.35	2846.2 ± 0.2	5350 ± 20	3180 ± 160
Mg II <sup>a</sup>	2803.53	2853.4 ± 0.2	5340 ± 20	3290 ± 150
Mg I	2852.96	2904.4 ± 0.2	5400 ± 20	1290 ± 120

**Note.** — The average velocity of this absorption-line system is 5360 ± 10 km s<sup>-1</sup>.

<sup>a</sup> This line is blended with Mg I  $\lambda$ 2853 absorption from the Galactic ISM.

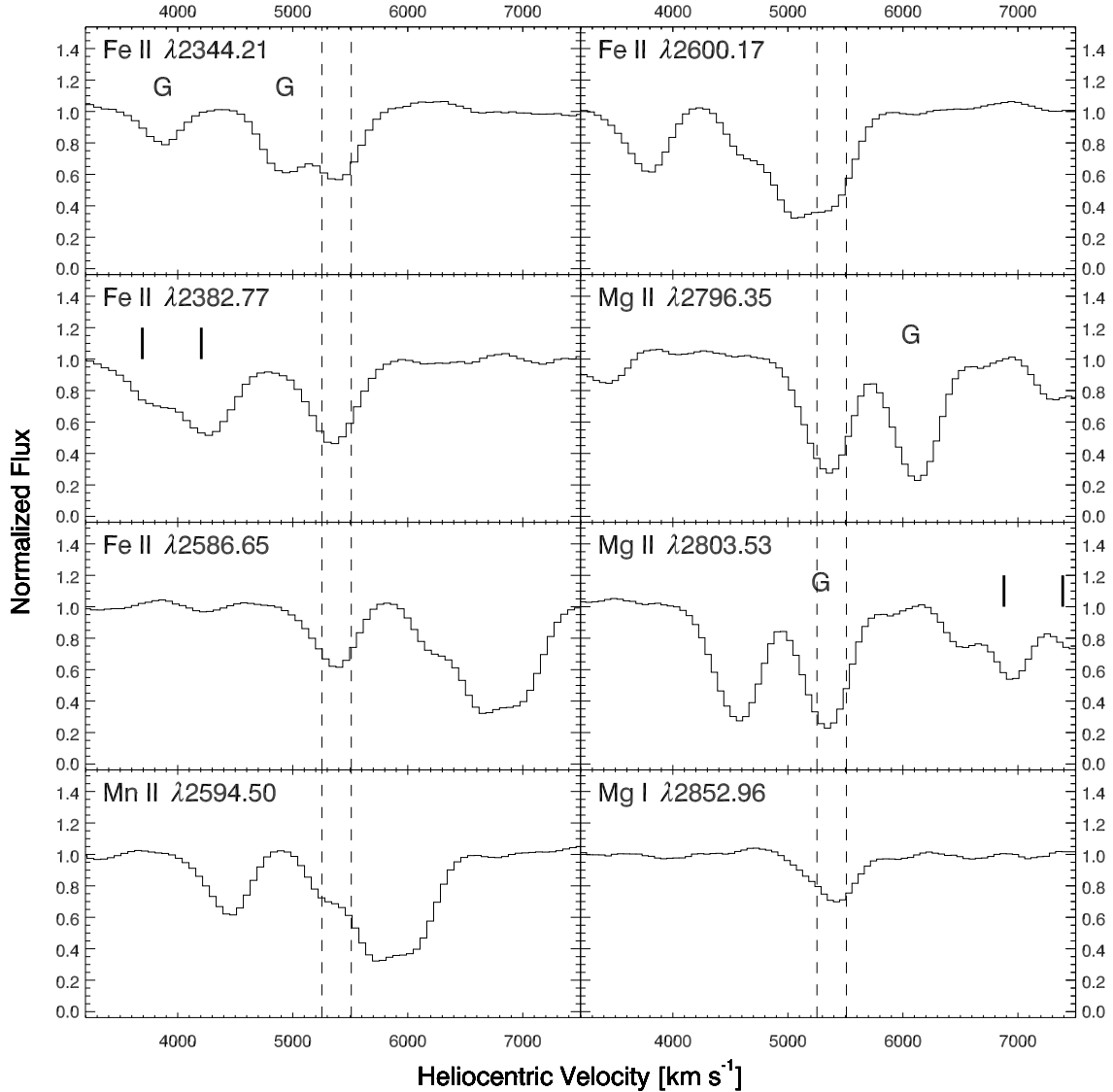


**Figure 6.** Absorption lines detected in the *HST*/FOS spectrum of PKS 1327–206 at the redshift of ESO 1327–2041. The species and rest wavelength of the line are labelled in the upper-left corner of each panel. The vertical dashed lines show the H I 21-cm absorption velocities (see Table 5). Positions of Galactic ISM absorption lines are marked with a “G” and lines associated with the LLS at  $z = 0.85238$  are marked with tick marks.

**Table 8**  
Galactic ISM Lines in the *HST*/FOS Spectrum of  
PKS 1327–206

ID	$\lambda_{\text{rest}}$ (Å)	$\lambda_{\text{obs}}$ (Å)	$v_{\text{helio}}$ ( $\text{km s}^{-1}$ )	$W_{\lambda}$ (mÅ)
Fe II	2344.21	$2344.6 \pm 0.2$	$50 \pm 30$	$1040 \pm 330$
Fe II	2374.46	$2374.4 \pm 0.2$	$0 \pm 30$	$570 \pm 130$
Fe II	2382.77	$2382.7 \pm 0.2$	$-10 \pm 30$	$1310 \pm 150$
Mn II	2576.88	$2577.3 \pm 0.3$	$50 \pm 30$	$1100 \pm 340$
Fe II	2586.65	$2586.7 \pm 0.2$	$10 \pm 20$	$840 \pm 270$
Mn II <sup>a</sup>	2594.50	$2595.9 \pm 0.2$	$160 \pm 20$	$2460 \pm 180$
Mg II	2796.35	$2795.6 \pm 0.2$	$-80 \pm 20$	$1500 \pm 170$
Mg II	2803.53	$2803.2 \pm 0.2$	$-30 \pm 20$	$1170 \pm 150$
Mg I <sup>b</sup>	2852.96	$2853.4 \pm 0.2$	$50 \pm 20$	$3350 \pm 150$

<sup>a</sup> This line is blended with an IGM Ly $\alpha$  absorber at  $z = 1.13536$ .

<sup>b</sup> This line is blended with Mg II  $\lambda 2804$  absorption from ESO 1327–2041.



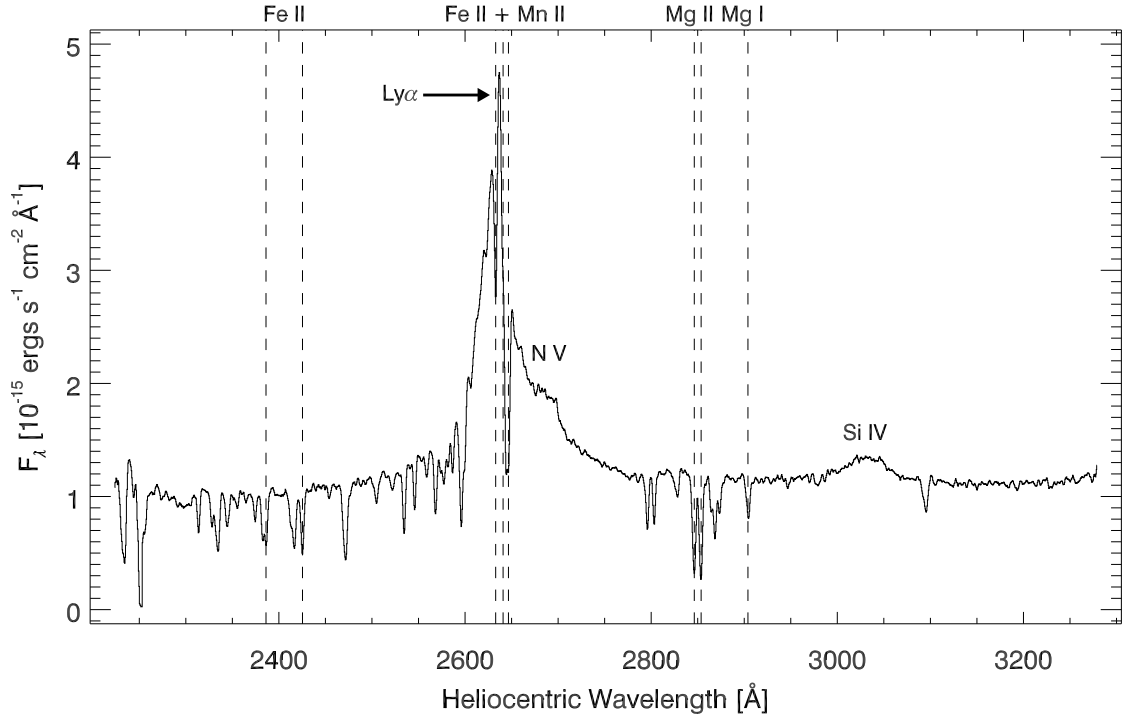


**Figure 7.** The full *HST*/FOS spectrum of PKS 1327–206. Quasar emission lines at  $z = 1.169$  are labelled and the positions of absorption lines associated with ESO 1327–2041 (see § 3.3 and Table 7) are indicated by the dashed vertical lines.

**Table 9**  
Lines Associated with the LLS in the *HST*/FOS Spectrum of  
PKS 1327–206

ID	$\lambda_{\text{rest}}$ ( $\text{\AA}$ )	$\lambda_{\text{obs}}$ ( $\text{\AA}$ )	$z$	$W_\lambda$ (m $\text{\AA}$ )
Si III	1206.50	$2233.3 \pm 0.1$	$0.85104 \pm 0.00004$	$1960 \pm 190$
Ly $\alpha$	1215.67	$2251.5 \pm 0.1$	$0.85203 \pm 0.00004$	$3270 \pm 400$
Si II	1260.42	$2334.2 \pm 0.1$	$0.85193 \pm 0.00004$	$1400 \pm 320$
O I	1302.17	$2412.8 \pm 0.1$	$0.85292 \pm 0.00005$	$580 \pm 50$
Si II <sup>a</sup>	1304.37	$2416.8 \pm 0.1$	$0.85286 \pm 0.00004$	$1060 \pm 50$
C II	1334.53	$2471.4 \pm 0.1$	$0.85187 \pm 0.00004$	$1610 \pm 90$
Si IV	1393.75	$2581.9 \pm 0.2$	$0.85249 \pm 0.00006$	$320 \pm 140$
Si IV	1402.77	$2599.7 \pm 0.1$	$0.85323 \pm 0.00004$	$390 \pm 70$
Si II	1526.71	$2827.7 \pm 0.1$	$0.85216 \pm 0.00005$	$380 \pm 90$
C IV	1548.20	$2868.5 \pm 0.1$	$0.85281 \pm 0.00004$	$910 \pm 80$
C IV	1550.78	$2873.5 \pm 0.1$	$0.85293 \pm 0.00004$	$550 \pm 80$
Al II	1670.79	$3094.9 \pm 0.1$	$0.85236 \pm 0.00004$	$630 \pm 70$

**Note.** — The average redshift of this absorption-line system is  $0.85238 \pm 0.00001$ .

<sup>a</sup> This line is blended with Fe II  $\lambda 2374$  absorption from ESO 1327–2041 but we attribute most of the absorption to Si II at  $z = 0.85286$ .

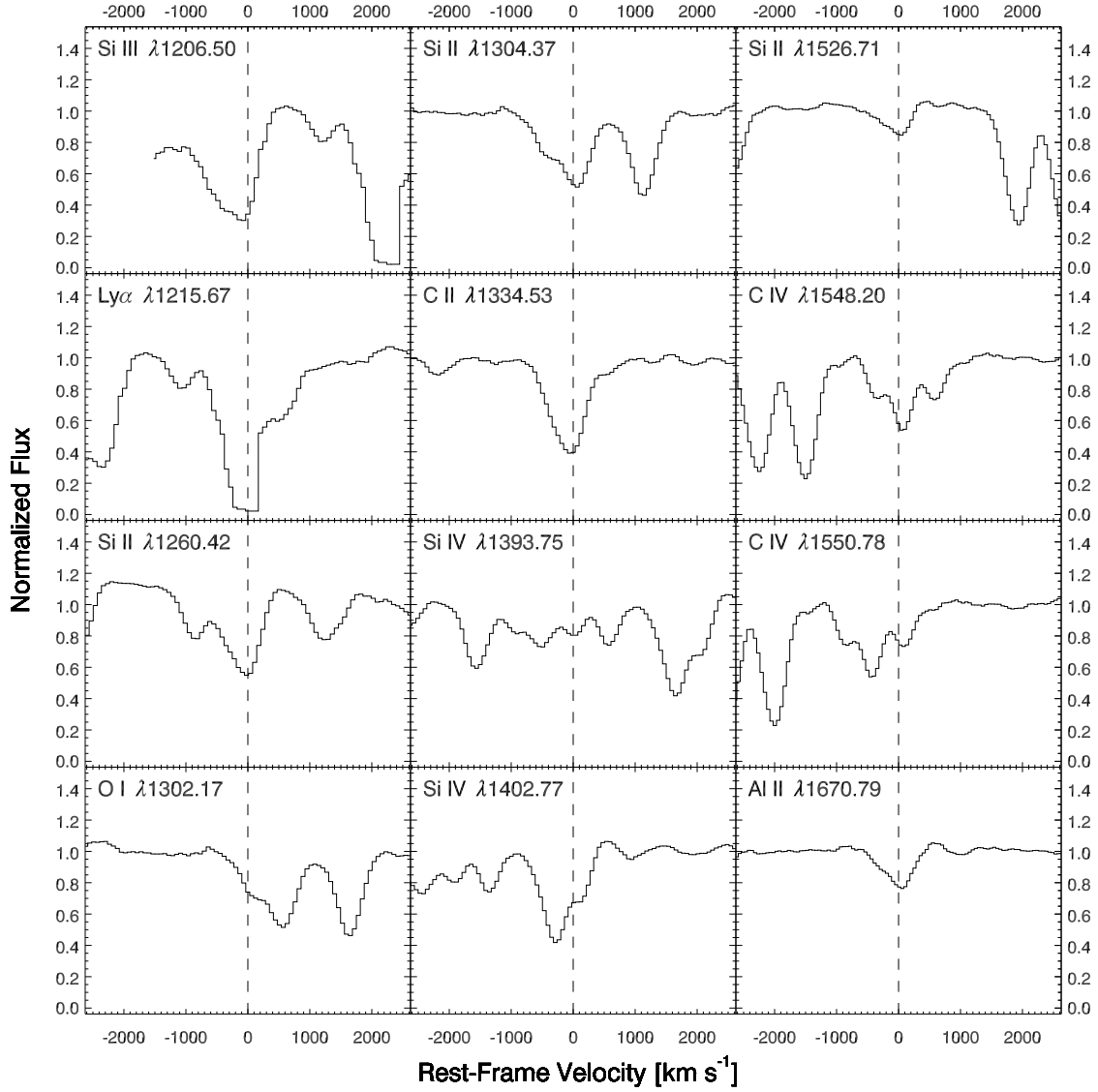


**Figure 8.** Absorption lines associated with the LLS at  $z = 0.85238$  in the *HST*/FOS spectrum of PKS 1327–206. The species and rest wavelength of the line are labelled in the upper-left corner of each panel. The vertical dashed line indicates a LLS rest-frame velocity of zero.

**Table 10**  
IGM Lines in the *HST*/FOS Spectrum of PKS 1327–206

ID	$\lambda_{\text{rest}}$ (Å)	$\lambda_{\text{obs}}$ (Å)	$z$	$W_{\lambda}$ (mÅ)
Ly $\alpha$	1215.67	2243.9 $\pm$ 0.2	0.84579 $\pm$ 0.00007	240 $\pm$ 140
Ly $\alpha$	1215.67	2256.7 $\pm$ 0.1	0.85637 $\pm$ 0.00005	460 $\pm$ 160
Ly $\alpha$	1215.67	2313.7 $\pm$ 0.1	0.90322 $\pm$ 0.00005	420 $\pm$ 110
Ly $\alpha$	1215.67	2328.6 $\pm$ 0.1	0.91547 $\pm$ 0.00005	360 $\pm$ 130
Ly $\alpha$	1215.67	2355.1 $\pm$ 0.3	0.93728 $\pm$ 0.00012	180 $\pm$ 100
Ly $\alpha$	1215.67	2454.1 $\pm$ 0.2	1.01875 $\pm$ 0.00006	170 $\pm$ 60
Ly $\alpha$	1215.67	2504.7 $\pm$ 0.1	1.06037 $\pm$ 0.00005	370 $\pm$ 80
Ly $\alpha$	1215.67	2521.9 $\pm$ 0.1	1.07452 $\pm$ 0.00006	230 $\pm$ 70
Ly $\alpha$	1215.67	2534.5 $\pm$ 0.1	1.08490 $\pm$ 0.00004	720 $\pm$ 60
Ly $\alpha$	1215.67	2545.9 $\pm$ 0.1	1.09421 $\pm$ 0.00004	420 $\pm$ 50
Ly $\alpha$	1215.67	2558.9 $\pm$ 0.1	1.10492 $\pm$ 0.00005	180 $\pm$ 100
Ly $\alpha$	1215.67	2568.3 $\pm$ 0.1	1.11270 $\pm$ 0.00004	730 $\pm$ 150
Ly $\alpha$	1215.67	2573.5 $\pm$ 0.2	1.11697 $\pm$ 0.00008	230 $\pm$ 120
Ly $\alpha$ <sup>a</sup>	1215.67	2595.9 $\pm$ 0.1	1.13536 $\pm$ 0.00004	1150 $\pm$ 80
C IV	1548.20	2864.5 $\pm$ 0.1	0.85021 $\pm$ 0.00004	430 $\pm$ 70

<sup>a</sup> This line is blended with Mn II  $\lambda$ 2594 absorption from the Galactic ISM.